JGR Solid Earth

RESEARCH ARTICLE
10.1029/2022JB024542

Detecting Preseismic Signals in GRACE Gravity Solutions: Application to the 2011 Tohoku M_w 9.0 Earthquake

Isabelle Panet[1,2], Clément Narteau[1], Jean-Michel Lemoine[3], Sylvain Bonvalot[4], and Dominique Remy[4]

[1]Université Paris Cité, Institut de Physique du Globe de Paris, CNRS, IGN, Paris, France, [2]ENSG-Géomatique, IGN, Marne-la-Vallée, France, [3]CNES, Géoscience Environnement Toulouse, CNRS, Université de Toulouse, Toulouse, France, [4]IRD, Géoscience Environnement Toulouse, CNRS, Université de Toulouse, Toulouse, France

Key Points:

- We develop a method to identify consistent solid Earth signals shared by different GRACE gravity models along plate boundaries
- The gravimetric preseismic anomaly of the 2011 Tohoku earthquake has a shape and magnitude that differ from all other signals
- Our method offers solutions for the continuous monitoring of deep slab gravity signals along the Pacific subduction belt

Correspondence to:
I. Panet,
panet@ipgp.fr

Citation:
Panet, I., Narteau, C., Lemoine, J.-M., Bonvalot, S., & Remy, D. (2022). Detecting preseismic signals in GRACE gravity solutions: Application to the 2011 Tohoku M_w 9.0 earthquake. *Journal of Geophysical Research: Solid Earth*, *127*, e2022JB024542. https://doi.org/10.1029/2022JB024542

Received 5 APR 2022
Accepted 31 JUL 2022

Abstract We conduct a global analysis of GRACE-reconstructed gravity gradients from July 2004 to February 2011, to test whether the deep signals preceding the March 2011 Tohoku earthquake can be detected before the event as a specific feature originating from solid Earth. First, we improve the angular resolution of the gravity gradients using two overlapping ranges of azimuthal sensitivity to investigate short-term signals of large amplitude aligned with the orientation of the Northwestern Pacific subduction. Then, we set-up a method to identify consistent solid Earth signals shared by different GRACE gravity models. Robust signals in a model are selected based on their spatial overlap and relative intensity with the signals of another model, so that their sensitivity to the GRACE data processing and ocean dealiasing product can be tested. We show that the dipolar gravity gradient anomaly before the Tohoku earthquake is nearly unique in space and time in the GRACE GRGS03 solutions. A well-resolved dipolar spatial pattern, typical of dislocations within the solid Earth and poorly sensitive to the ocean dealiasing model, is detected. In addition, the preseismic gravity gradient increase is highly consistent between the GRGS03 and CSR06 solutions, independently from their respective oceanic corrections, and can be clearly distinguished from rare anomalies of similar amplitudes all associated with the water cycle over continental areas. Our approach offers solutions for the continuous monitoring of the Pacific subduction belt to document transient slabs motions in real time from global satellite gravity fields, and their relation with shallower deformations and seismic events.

Plain Language Summary Retrieving short-term preseismic signals before the occurrence of great subduction earthquakes is a major goal for seismic hazard mitigation. It requires a continuous monitoring of the deformations within the entire subduction system, from surface to depth along the descending slab. Space geodesy and seismicity provide monitoring of seismic events and shallower aseismic motions, but the full spectrum of transient deformations of the pulling slab at depth remains mostly unknown. Their detection is crucial, as they might precede shallower deformations and foreshocks that would result from their upward propagation. Time-varying satellite gravity can overcome this observational limit, thanks to a unique sensitivity to mass redistributions at all depths and a global coverage. Here, we develop a method to identify solid Earth signals along plate boundaries in the time series of GRACE geoid models. It is based on a refined detection of signals aligned with the subduction direction, and consistency tests between signals shared by different sets of geoid models. The results underline the unique nature of the preseismic signals of the 2011 Tohoku earthquake with respect to water cycle contributions and noise. Our approach thus offers an opportunity for the continuous monitoring of deep mass redistributions at subduction zones.

1. Introduction

Subduction earthquakes are devastating events causing considerable damage in often densely populated areas. Retrieving preseismic signals remains a critical challenge of Earth's sciences, which calls for a better understanding of the different types of deformations at subduction zones and their interactions. From continuous slip along creeping segments to earthquake ruptures, seismic and geodetic data have revealed a diversity of transient motions. Near the seismogenic zone along the plates interface, they include slow slip events at timescales from days to years, seismic slow earthquakes at timescales of 10s of seconds, and a wide range of tremor activity at periods of 0.1s seconds (Obara & Kato, 2016; Schwartz & Rokosky, 2007). They suggest the existence of various slip behaviors between fast ruptures and long-term stable sliding, but how they may interact with giant earthquakes is not well understood. At the same time, seismic data and models of stress redistribution during

the seismic cycle underline the relation between deformations in the deeper descending slab and at the plates interface (Astiz et al., 1988; Dmowska et al., 1988). However, the full spectrum of aseismic deformations of the subducted slab at depth remains mostly beyond the reach of seismic and geodetic observations, and there is no access to an important component in the balance of forces applied to the downgoing plate.

In this context, the early identification of preseismic signals of an impending earthquake has remained elusive. Over the short term, retrospective analyses have evidenced deep and shallow deformation transients at timescales from days to decade before great subduction earthquakes. These transients include migrations of seismicity in the subducted slab down to the transition zone, from months to years prior to great shallow earthquakes (Dmowska et al., 1988; Mogi, 1973, 2004), or synchronized seismicity at shallow and intermediate depth in the months before recent megathrusts suggesting that the ruptures have been preceded by broad slab deformations (Bouchon et al., 2016). Earthquake swarms may also trigger unstable slip at coupled plate interfaces (Nishikawa & Ide, 2018; Ruiz et al., 2014). Space-geodetic data furthermore recorded accelerated deformations of the upper plate prior to recent great subduction events. In Japan, a reduction in the plates interface coupling was observed at decadal timescale before the 2011 Tohoku earthquake (Mavrommatis et al., 2014; Yokota & Koketsu, 2015), together with slow slip activity in the vicinity of the rupture zone in the month before the mainshock (Ito et al., 2013). In North Chile, slow slip surrounding the coseismic rupture patch appeared 8 months before the 2014 Iquique earthquake (Socquet et al., 2017). These seismic and geodetic preseismic events (Hasegawa & Yoshida, 2015) suggest interactions between deeper and shallower deformation processes at different timescales prior to the occurrence of great subduction earthquakes.

With a sensitivity to mass redistributions at all depths and a temporal resolution of days to 1 month, GRACE and GRACE Follow-On satellite gravity data (Tapley et al., 2004) naturally complement the seismic data and the space-geodetic observations of ground displacements. They seem particularly well adapted to decipher deeper deformations in the subduction system that could potentially precede shallower ones. Shahrisvand et al. (2014) thus reported anomalously large variations in time series of the spatial gradients of the Earth's gravity field in the weeks before three major earthquakes (the 2010 Maule, the 2011 Tohoku, and the 2012 Indian ocean earthquakes). More recently, we identified and mapped in space and time anomalous variations in Earth's gravity gradients during the months preceding the ruptures of the 2011 Tohoku earthquake (Panet et al., 2018) and the 2010 Maule earthquake (Bouih et al., 2022). We showed that they result from a deep, broad deformation of the subducted slab beneath the lithosphere, providing favorable conditions for the occurrence of the giant earthquake as this deformation migrated from depth to the surface. These results are corroborated by an analysis of GNSS data, which exhibits geodetic preseismic signals at the same spatial and temporal scales as the gravitational anomalies (Bedford et al., 2020). In the case of the Tohoku earthquake, they suggest a sudden pull-down of the Philippine Sea slab before the event, followed by an accelerated Pacific slab plunge. All these studies raise the question whether anomalous gravity gradient variations at subduction zones could be automatically detected in the satellite gravity data before giant earthquakes, as real time indicators for sudden motions of the slabs at depth.

In the GRACE data, the gravity variations caused by mass redistributions associated with deeper slab motions are in a vast majority of cases smaller than the contributions from the water cycle in the Earth's fluid envelopes and from the noises. Furthermore, their identification should be performed continuously all over the globe to contribute to the characterization of seismic hazard along the Pacific subduction belt. Based on the novel observation of Panet et al. (2018), this question is addressed in the case of the Tohoku earthquake by Wang and Bürgmann (2019). They conducted a statistical analysis of the GRACE-based gravity gradients all over the globe in order to test whether the preseismic changes could be systematically recognized as a distinctive feature compared to the natural variability of the gravity field. Because the preseismic signal of the Tohoku earthquake appeared statistically nonunique, the authors concluded that it could not be significantly regarded as originating from the solid Earth. Here, we extend this work and conduct a statistical analysis to identify robust anomalous solid Earth signals aligned with the orientation of a plate boundary at the subannual timescales of fast geodetic, seismic, and gravitational preseismic signals reported in previous studies (Bedford et al., 2020; Bouchon et al., 2016; Bouih et al., 2022; Panet et al., 2018). First, we enhance the geometric analysis of the gravity gradients variations in order to extract signals aligned with a chosen plate boundary orientation, as expected for subduction mass transfers (Section 3). This way we introduce an important geological constraint in our analysis of the signals. Then, to evaluate the significance of the obtained short-term gravity gradient anomalies, we design a method to select consistent signals shared by different GRACE gravity field solutions and assess their

sensitivity to the ocean mass model used in the dealiasing of the GRACE observations (Section 4). We apply our approach to the case of the 2011 Tohoku earthquake, to show that the preseismic gravity gradient variation presented in Panet et al. (2018) can be efficiently isolated and automatically retrieved from global satellite gravity datasets before the occurrence of the earthquake (Section 5). Finally, we discuss how the uniqueness of the Tohoku preseismic anomaly lies in its shape and magnitude, representative of solid Earth processes (Section 6).

2. Data

2.1. The GRACE Geoid Models

We use two sets of GRACE geoid models, also called *solutions*, provided by different analysis centers and expressed as spherical harmonics expansions: the GRGS Release 3 up to degree/order 80 (Bruinsma et al., 2010; Lemoine et al., 2007) and the CSR Release 6 up to degree/order 96 (Bettadpur, 2018a, 2018b). A DDK6 destriping filter (Kusche et al., 2009) is applied to the CSR06 geoids as a postprocessing step, to reduce the striping artifacts oriented along the orbit (mainly in the North-South direction). Fast variations of the gravity field need to be removed from the original observations in order to minimize their aliasing in the monthly geoids. This is done using background geophysical models for tidal mass redistributions, nontidal atmospheric mass changes and ocean response to the atmospheric pressure and winds forcing (Dobslaw et al., 2017; Gégout et al., 2009). To assess the robustness of the identified signals with respect to the ocean correction, we use two sets of geoid models: the *standard, ocean-removed* solutions, from which the dealiasing ocean mass model has been removed, and the *ocean-restored* solutions, where this ocean contribution has been restored (see Section 4). If not specified, we implicitly refer to the standard, ocean-removed solutions. Note that, due to a change between the Releases 5 and 6 of the dealiasing products for the CSR geoids, the atmospheric contribution over the oceans is added to the CSR dealiasing ocean mass model. This results in a reduced variability, reflecting the inverse barometer response of the ocean to atmospheric pressure variations.

2.2. Differences Between the GRGS03 and the CSR06 Solutions

The estimation of these geoid models relies on a numerical integration of the dynamical equations of motion of the GRACE satellites, which orbital perturbations reflect the forces acting on the spacecrafts, including the Earth's gravitational attraction. The orbit adjustment requires the resolution of a nonlinear system. In order to linearize the observations equations, the geoid models are estimated as updates with respect to a reference gravity field model. For both CSR and GRGS solutions, this reference gravity model includes a mean static field, and a priori knowledge on its temporal variations based on the background geophysical models mentioned above and empirical determinations of a secular trend. For the GRGS solution, additional biases and periodic annual components are introduced. Errors on the modeled submonthly signals result in periodic aliases in the monthly geoids (Ray & Luthcke, 2006). Errors on the reference gravity field at longer timescales are not expected to perturb significantly the solution unless a regularization constraint is applied. The main differences between the GRGS and the CSR approaches involve:

1. *Different Background Geophysical Models for the Nontidal Atmospheric and Oceanic Mass Changes*. The GRGS solution uses the ECMWF ERA-Interim atmospheric pressure fields (Dee et al., 2011), and the barotropic TUGO ocean mass model (Carrère & Lyard, 2003). The CSR solution uses the AOD1B RL06 mass variability model (Dobslaw et al., 2017), based on the same atmospheric pressure fields up to the year 2006 and on operational ECMWF analyses for the subsequent years, and the Max-Planck-Institute for Meteorology Ocean Model (MPIOM) ocean mass model (Jungclaus et al., 2013).
2. *Different Weightings of the Observations*. The C_{20} spherical harmonics coefficient of the geoid must be constrained from Satellite Laser Ranging (SLR) data, more precise than GRACE at these global scales. The GRGS solution jointly inverts SLR and GRACE data to ensure consistent temporal variations of the spherical harmonics coefficients over a range of low degrees/orders. In the CSR solution, this coefficient is substituted with an independent SLR-based determination, which may involve different processing standards. Another difference concerns the combination of the GPS tracking of the satellite orbits with the K-Band Range (KBR) measurements of the inter-satellite range and range-rate variations. The GPS data constrain the geoid models only up to degree/order 40 in the GRGS solution, against 96 in the CSR solution.

3. *Different Least Squares Inversion Strategies*. The GRGS develops a two-step inversion regularized by a Truncated Singular Value Decomposition (TSVD) approach, for which no prior geophysical model is required (Lemoine et al., 2016). The first step is dedicated to the estimation of the lower degrees of the gravity field from a classical Cholesky inversion. Only the degrees from 2 to 30 are solved, applying a Kaula-type regularization from degrees 5 to 30 to express the decay of the gravity field spectrum (Kaula, 1966). In the second step, updates with respect to the obtained spherical harmonics coefficients are estimated from a TSVD decomposition of the normal matrix, except for degree 2 which is fixed to the solution of the first step. The TSVD accounts for 97% of the data variance, corresponding to about 50% of the singular values set to zero. Note that solving for the complete set of eigenvectors would be equivalent to a Choleski inversion, accounting for 100% of the data variance. Instead of constraining the coefficients individually, as done in regularizations involving a prior covariance matrix, the TSVD constrains only linear combinations of coefficients, which offers more flexibility on the solution. Without any regularization, the CSR inversion provides fully unconstrained solutions affected by a higher level of striping artifacts than the GRGS solutions. This is why directional destriping filters are applied to the CSR solutions, also removing the entire North-South components of the signals at the spatial resolution of the filters.

3. Gravity Gradients Space-Time Analysis

To study the anomalous character of the gravity variation before the 2011 Tohoku earthquake, we extract from the total field the fast gravity signals of large amplitude, with elongated shapes oriented along the direction of the Northwestern Pacific subduction zone. Compared to the methodologies used in Panet (2018) and Panet et al. (2018), here we further develop the space-time analysis of the gravity gradients in order to enhance the azimuthal sensitivity of the gradients (Section 3.1.2) and isolate their variations at short timescales (Section 3.2).

3.1. Spatial Analysis

3.1.1. Multiscale Gravity Gradients

Our analysis of the spatial variations of the gravity field is based on a multiscale description of gravity gradients built from the monthly GRACE geoids (see Panet, 2018, and references therein for details). The principle is to extract the geoid variations at different spatial scales from the total geoid using spherical wavelet filtering, and then, to reconstruct at each scale s the gravity gradient tensor in the local spherical frame from the wavelet-filtered geoid. In geocentric Cartesian coordinates, these gradients correspond to the second-order spatial derivatives of the gravity potential in the three directions of space; they are expressed in spherical coordinates through appropriate coordinate transformations.

We focus on the horizontal gradients, which enhance structures orthogonal to the horizontal basis vectors of the local spherical frame $\left(\vec{e}_r, \vec{e}_\theta, \vec{e}_\phi\right)$. To highlight signals following the direction of subduction boundaries, which can be different from North-South or East-West, we rotate the local spherical frame along the radial axis by an angle denoted Az. With the chosen notation, we amplify signals along the Az or the $Az + 90°$ azimuth depending on the choice of the $\phi\phi$ or $\theta\theta$ component of the gravity gradient tensor. This way, superimposed signals generated by different mass sources can be identified as a function of their size and orientation.

3.1.2. Rotations of the Spherical Frame and Improvement of the Angular Resolution

We consider two sets of rotation angles of the local spherical frame: the sets Az_1 and Az_2 spanning the 20–55° and 60–85° clockwise rotations of the frame, respectively. These rotations correspond to azimut ranges of 20–55° and 60–85° for the extracted $\phi\phi$ gravity gradients signals respectively. We stack the horizontal $\phi\phi$ gravity gradients over all rotation angles within each set to increase the signal-to-noise ratio for signals with orientations close to $\overline{Az}_1$ and $\overline{Az}_2$, the centers of these intervals (azimuts 37.5°E and 72.5°E). We perform two types of analyses:

1. *Degraded Analysis*. we focus on the gravity gradients obtained for the Az_2 range. This set of directions allows us to minimize the impact of the striping noise because the azimuth of the extracted $\phi\phi$ gravity gradients signals is oblique to the North-South striping orientation. In addition, the Az_2 range remains close enough to the orientation of the Northwestern Pacific subduction to ensure the detection of the signals aligned with this plate boundary.

2. *Optimal Analysis*. we combine the gravity gradients obtained for the Az_1 and Az_2 ranges, in order to enhance the directional sensitivity along the orientation of the Northwestern Pacific subduction system. The principle is to search for gravity gradient anomalies simultaneously detected by two overlapping ranges of azimuthal sensitivity to isolate signals aligned with this angular overlap.

The *optimal analysis* is illustrated in Figure 1 using an elongated source with a length-to-width ratio of 4. When we compute its horizontal gravity gradients in a rotated frame, we obtain a maximum amplitude above the source for a frame aligned with the source main axis. For instance, in the left column of Figure 1, the spherical frame orientation is fixed to the Az_1 azimuth range and the mass source is progressively rotated as shown in the right column. The obtained gravity gradient anomaly can be detected when the average frame orientation $\overline{Az}_1$ is within $\pm 45°$ around that of the source (red panels contours), with a decreasing amplitude for increasing differences in orientation between the source and the frame. For a $\pm 45°$ orientation difference, the amplitude above the source is divided by a factor of ~ 3 as compared to its extreme value whatever the aspect ratio of the source (not smaller than 2). Thus there is a $\left[\overline{Az}_1 - 45°E; \overline{Az}_1 + 45°E\right]$ angular sensitivity interval of the $\phi\phi$ gravity gradients. Note that in this interval, the orientation of the gravity gradients signal remains close to that of the source within a few degrees only. This behavior of the gravity gradient signals is described in detail in Panet (2018).

Let us now consider the analysis of real gravity data. When we focus on a chosen orientation for the spherical frame, we enhance gravity gradient signals aligned with this direction, but also capture other signals oriented within $\pm 45°$ of this direction, still detectable in a nonoptimal configuration of the frame if their amplitude is large enough. Searching for anomalous gravity gradient variations jointly detected in the two azimuthal ranges Az_1 and Az_2, we extract the signals which orientation belongs to the intersection of the two associated intervals of angular sensitivity. In the example of Figure 1, these intervals are marked by the red and blue panel contours. Thus the angular resolution is enhanced from 90° to 55°, the width of the overlapping sensitivity interval $\left[\overline{Az}_1 - 45°E; \overline{Az}_1 + 45°E\right] \cap \left[\overline{Az}_2 - 45°E; \overline{Az}_2 + 45°E\right]$. The anomalous gravity gradient variations detected in both the Az_1 and Az_2 directions are combined through averaging; this way, we are able to extract elongated signals with an improved angular resolution. Note that we also extract circular, "bell-shaped" signals because the amplitude of the horizontal gravity gradients of these isotropic structures does not vary much with direction (see Panet, 2018, Figure 14), hence they are detected in all directions.

Considering satellite gravity data, the degraded and optimal analyses can both be performed on the GRGS solutions, because of their lower level of North-South striping artifacts. In contrast, the CSR solutions can only be analyzed using the Az_2 range and the degraded analysis to ensure a proper separation of the signals from the striping noise.

3.2. Temporal Analysis

We have obtained time series of gravity gradients for the Az_1 and Az_2 azimuth ranges, at different spatial scales s. These time series are truncated in February 2011, so that our analysis is carried out without any knowledge about the occurrence of a giant earthquake. From January 2003 to December 2009, we estimate periodic components associated with the annual, the semiannual and the 161-day alias of the S2 oceanic tides, and remove them from the time series. Then, we search for anomalously large gravity gradient variations at timescales of a few months (less than 1 year). To smooth out the time series and focus on the fast residuals, we apply a temporal running average with a duration of N-months. This filter optimally reduces random white noise in the time series, at the cost of a degraded localization in frequency (Smith, 1998). This last point is however not critical, because we have already corrected the time series for most of the periodic variations and we investigate spike-like or step-like signals rather than oscillating behaviors. More importantly, the compact support in the time domain of the running average improves the smoothing at the end of the time series compared to other filters showing a better frequency localization at the cost of a broader temporal support.

Indeed, the running window cannot be implemented over the final $N/2$-month time interval due to the finite length of the time series. We thus implement a constant extrapolation of the smoothed time series, so the last value averaged over a complete N-months long interval applies for this final period, as illustrated in Figures 2a and 2c for February 2011. As the length of the extrapolation interval is minimal for the running average compared to other

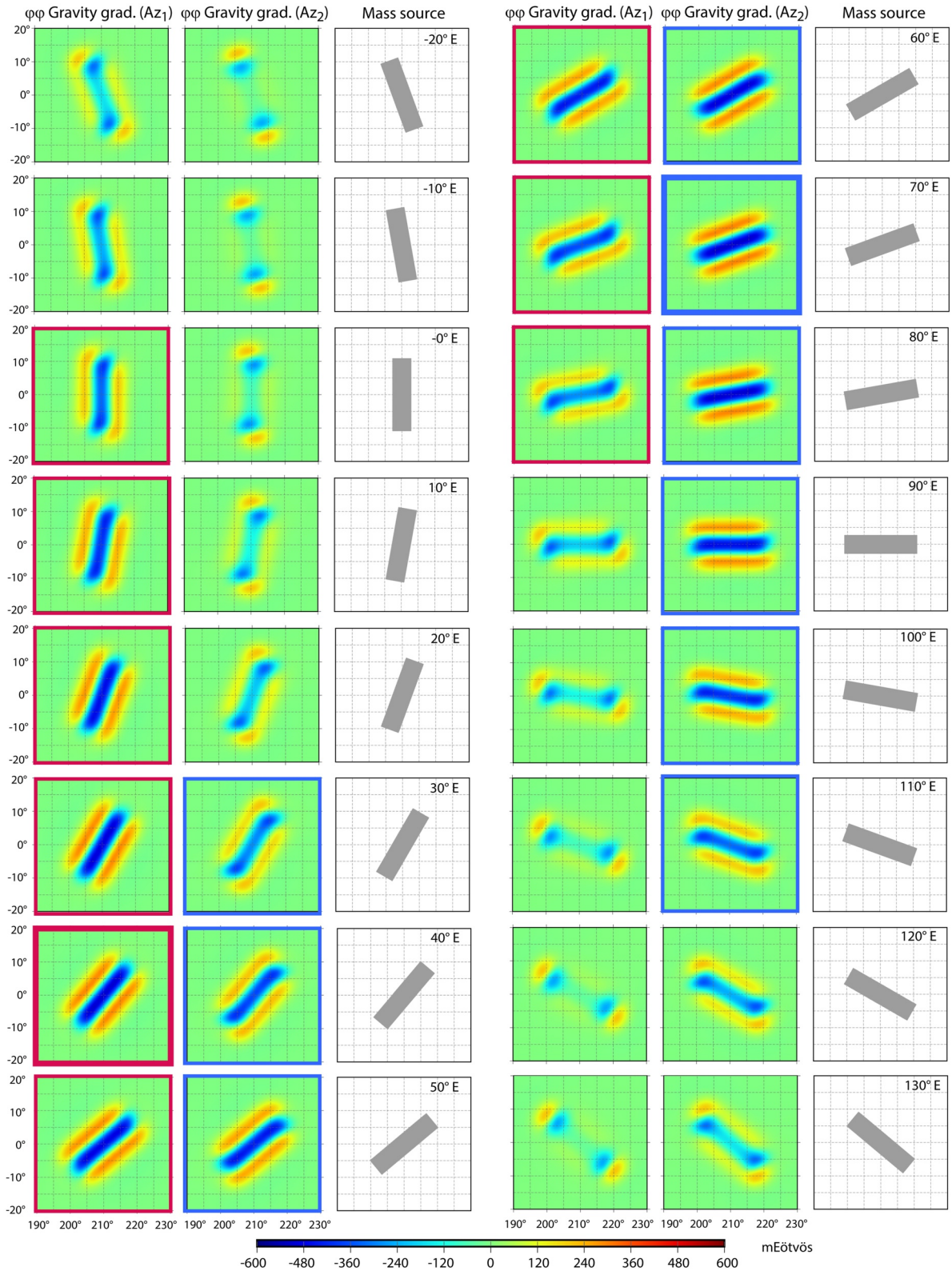
φφ Gravity grad. (Az1)
φφ Gravity grad. (Az2)
Mass source
-20° E
-10° E
-0° E
10° E
20° E
30° E
40° E
50° E
60° E
70° E
80° E
90° E
100° E
110° E
120° E
130° E
20°
10°
0°
-10°
-20°
190° 200° 210° 220° 230°
-600 -480 -360 -240 -120 0 120 240 360 480 600
mEötvös

Figure 1.

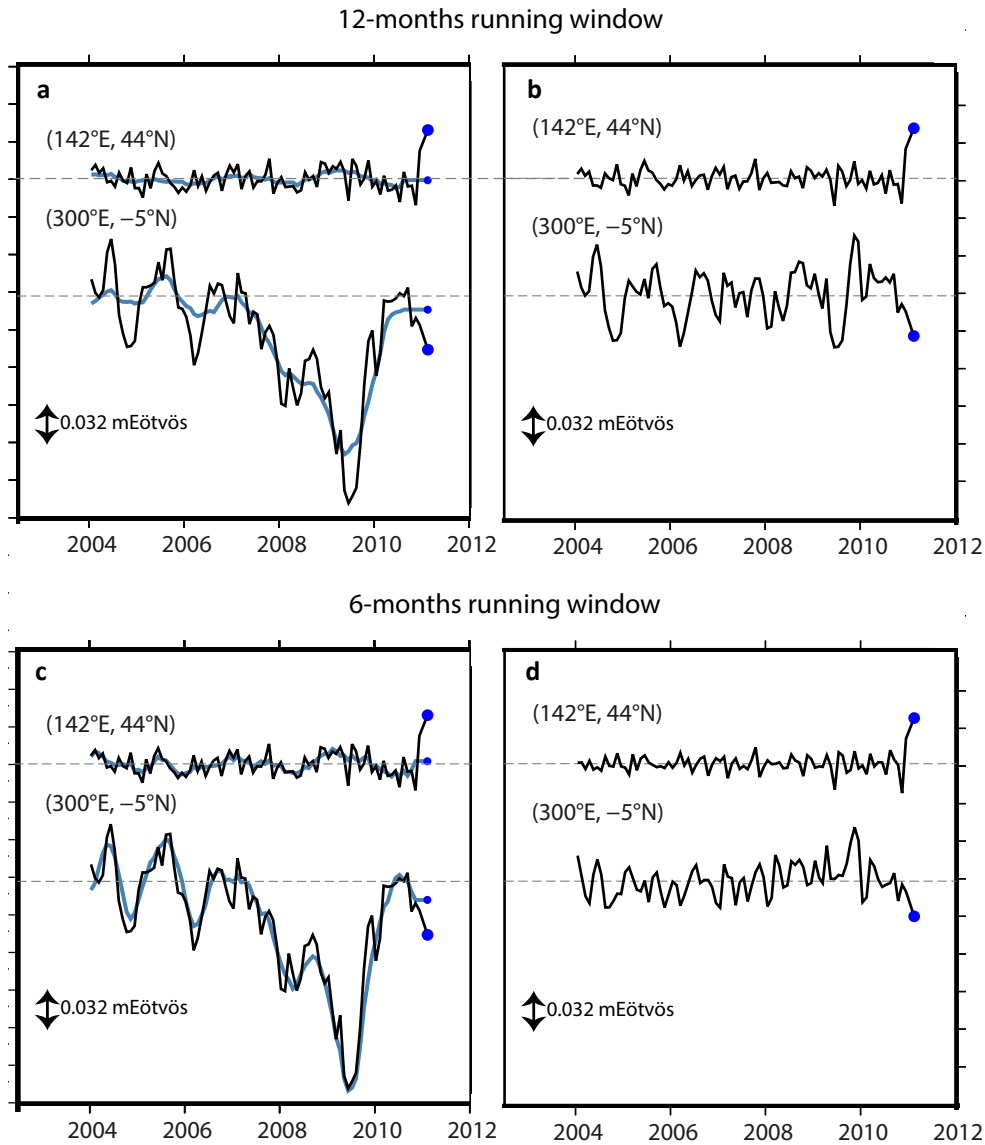

Figure 2. Extraction of the fast variations in the time series. (a, c) Gravity gradient time series (1,400-km scale $\phi\phi$ gravity gradients, Az_2 azimuth range) in Northern Japan and in the Amazon basin (black curves), and their smooth variations obtained by applying temporal running windows with a duration of 12-month (a) and 6-month (c), and a constant extrapolation over the final 6-month and 3-month intervals, respectively (blue curves). (b, d) Short-term residuals $\tilde{g}_6(t)$ and $\tilde{g}_{12}(t)$ obtained by removing these smooth variations from the time series. Blue dots show values in February 2011.

filters, we can show that the error due to neglecting the smooth variations over this final $N/2$ months interval is small around Japan in February 2011 (Appendix A). We denote $\tilde{g}_N(t)$ the obtained short timescale residuals (Figures 2b and 2d).

We have applied this temporal filtering for a range of running windows, varying N from 2 to 18 months. For shorter durations ($N = 2$ or 4 months), the residuals are dominated by the random noise of the time series. For longer durations ($N = 18$ months), the residuals contain an increasing number of "slower" signals. To avoid the predominance of these noises or these slower variations in the residual time series and isolate signals at

Figure 1. Enhancing the angular resolution of the gravity gradients using overlapping azimuthal ranges (optimal approach). $\phi\phi$ gravity gradient signals of an elongated mass excess source of aspect ratio 1:4, expressed in the local south-east-up spherical frame of unit vectors (e_θ, e_ϕ, e_r), rotated in the direction Az_1 (column 1) or Az_2 (column 2), for different orientations of the source from −20°E to 130°E (column 3). The scale of the gravity gradients corresponds to the width of the source (1,000 km). Red (resp. blue) frames: angular sensitivity intervals of the gravity gradients for the Az_1 (resp. Az_2) orientations of the south-east-up spherical frame (i.e., the signal amplitude above the source exceeds half its maximum value, marked by the thicker red and blue frames).

timescales of a few months, we consider durations N equal to 6 and 12 months and we search for anomalous time signals in both residual time series, $\tilde{g}_6(t)$ and $\tilde{g}_{12}(t)$. By definition, these anomalies correspond to extreme values under an assumption of a Gaussian distribution of the residuals $\tilde{g}_N(t)$. At each spatial grid point, the mean and standard deviation of the reference distribution are computed over the July 2003 to February 2010 reference period. Temporal signals outside the [1–99%] (resp. [5–95%]) percentiles of the reference distribution for the GRGS (resp. CSR) gravity solutions are defined as anomalies. The slightly different thresholds reflect different noise levels in the two solutions. At each point in space and time, the temporal anomalies detected in both $\tilde{g}_6$ and $\tilde{g}_{12}$ are averaged, otherwise the value of the gravity gradient is set to zero. This way we build at each time t a spatial map of anomalous gravity gradient signals.

4. Methodology to Identify Consistent Signals Between Different Gravity Models

The analysis described in Section 3 provides a sequence of maps of anomalous gravity gradient signals at the different times t, in a chosen azimuth range Az and for a spatial scale s. To evaluate the significance of individual anomalies, we assess their consistency across different gravity solutions and their sensitivity to the ocean models used in the dealiasing of the GRACE observations. In what follows, a so-called "gravity field model" corresponds to the choice of:

1. A gravity solution (CSR06 or GRGS03).
2. The removal (standard solutions) or the restoration of its dealiasing ocean model.

We end-up with four different gravity field models that can be compared to one another.

Let us consider two such anomaly maps $\mathcal{A}(t, Az, s)$ and $\mathcal{B}(t, Az, s)$, obtained from two gravity field models and expressed in terms of their gravity gradients $\tilde{g}_\mathcal{A}$ and $\tilde{g}_\mathcal{B}$. Using the regular grid in latitude and longitude, a cluster analysis based on nearest and next-nearest neighbors identifies and counts the individual signals A_i and B_j in each map, where $i \in [1, N_A]$ and $j \in [1, N_B]$. N_A and N_B are the number of signals in the maps $\mathcal{A}$ and $\mathcal{B}$, respectively. The principle is to identify in the map contiguous groups of grid cells associated with nonzero values and surrounded on all sides by grid cells with zero values, where adjacent grid cells share a side or a corner. Such algorithms are used in computer vision to detect connected regions in an image (Haralick & Shapiro, 1992). The cluster analysis also gives the surface, the integrated amplitude (or magnitude) and the coordinates of the barycenter of each signal (Table 1). Then, in order to search for common signals in $\mathcal{A}$ and $\mathcal{B}$, we design a simple method to evaluate the consistency in spatial extent and amplitude between pairs of anomalies $\{A_i, B_j\}$, considering only overlapping pairs of similar sign. Each pair is characterized by its overlap area (see Figure 3a) and the spatial properties of the overlaps are derived as done for the individual signals (Table 1).

Table 1
Properties of the Individual Clusters (Left) and the Overlaps (Right)

Spatial properties of the clusters and overlaps			
No.	Variable	No.	Variable
01	Number of the cluster	01	Number of the cluster 1
02	Number of pixels	02	Number of the cluster 2
03	Intensity	03	Sign of the overlap
04	Surface	04	Surface of the overlap
05	Mean intensity	05	Intensity of the overlap 1
06	Mean latitude	06	Intensity of the overlap 2
07	Mean longitude	07	Surface overlap ratio 1
		08	Surface overlap ratio 2
		09	Intensity overlap ratio 1
		10	Intensity overlap ratio 2

We characterize an overlap between two spatial anomalies using two parameters:

1. The *relative overlap intensity* k: it gives the amplitude ratio of the two signals A_i and B_j within their overlap zone $O_{ij} = A_i \cap B_j$:

$$k_{ij} = \frac{\int_{O_{ij}} (\tilde{g}_\mathcal{A}(\theta, \phi) - \tilde{g}_\mathcal{B}(\theta, \phi))\, \mathrm{d}\sigma(\theta, \phi)}{\int_{O_{ij}} \tilde{g}_\mathcal{B}(\theta, \phi) \mathrm{d}\sigma(\theta, \phi)} \quad (1)$$

where θ is the colatitude, ϕ the longitude, and $\mathrm{d}\sigma$ the surface element on the Earth's mean sphere.

2. The *individual overlap fraction* S: it measures the fraction of the total magnitude of a signal A_i (resp. B_j) that overlaps with another signal B_j (resp. A_i):

$$S^A_{ij} = \frac{\int_{O_{ij}} \tilde{g}_\mathcal{A}(\theta, \phi) \mathrm{d}\sigma(\theta, \phi)}{\int_{A_i} \tilde{g}_\mathcal{A}(\theta, \phi) \mathrm{d}\sigma(\theta, \phi)} \quad (2)$$

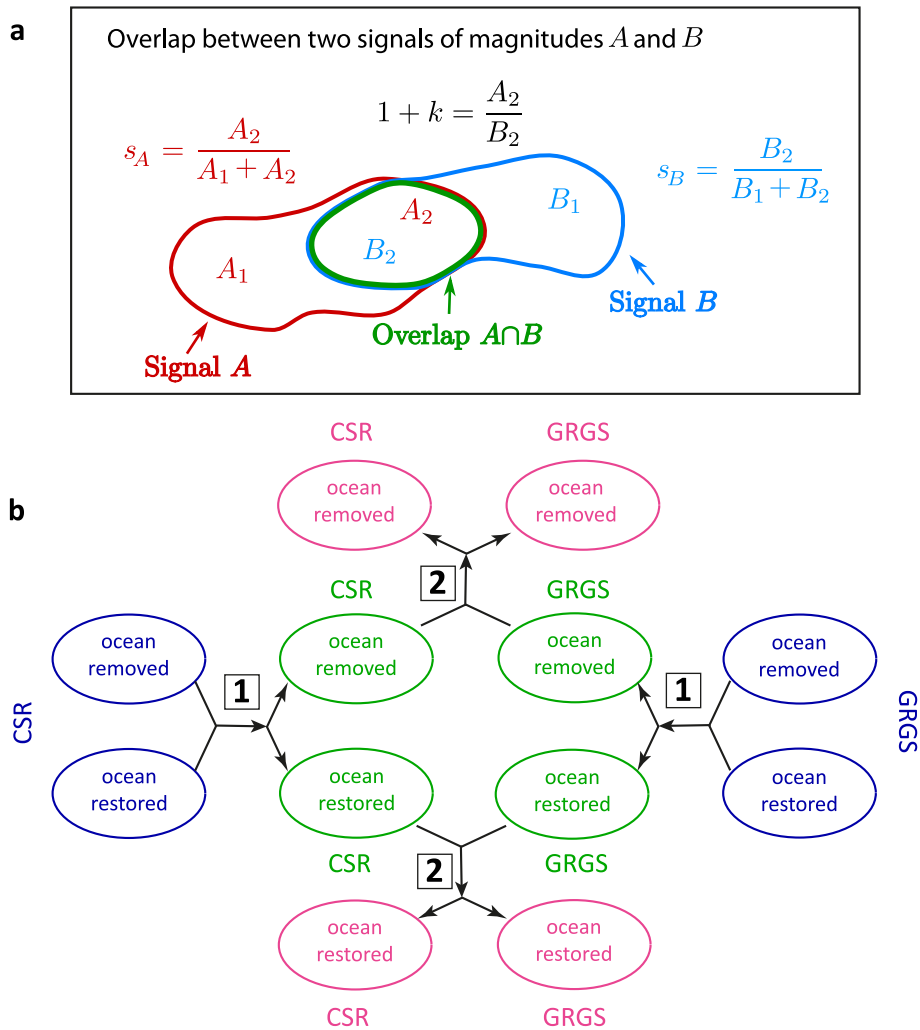

Figure 3. Assessing the consistency between different gravity models. (a) Definition of the k and S parameters to characterize the consistency between two signals from two different gravity models (in red and blue), of respective magnitudes $A = A_1 + A_2$ and $B = B_1 + B_2$ where A_2, B_2 are the magnitudes in the overlap zone (in green). (b) Comparisons of different gravity models to assess the robustness and origin of the signals. Signals poorly sensitive to the ocean model are identified from the consistency between GRACE gravity solutions of the same group, with or without restoration of the ocean dealiasing model (1). Signals poorly sensitive to the methodology used to build the GRACE gravity models from the original observations are identified from the consistency between different GRACE gravity solutions (2). The successive application of these two selections points to the signals consistent between different GRACE gravity solutions and poorly sensitive to their respective ocean dealiasing models.

$$S_{ij}^{B}=\frac{\int_{O_{ij}}\tilde{g}_B(\theta,\phi)\mathrm{d}\sigma(\theta,\phi)}{\int_{B_j}\tilde{g}_B(\theta,\phi)\mathrm{d}\sigma(\theta,\phi)} \tag{3}$$

While k informs on the difference in amplitude between A_i and B_j in their overlap zone, S characterizes their geographic coincidence. k close to 0 indicates similar amplitudes in the overlap (identical if $k = 0$); S close to 1 indicates a large overlap, which includes the whole signal if $S = 1$. Thus, a high geographic coincidence results in high values (close to 1) of both S_{ij}^{A} and S_{ij}^{B}. The case where the surfaces of two overlapping signals are very different, for instance when the surface of A_i is much smaller than that of B_j, is reflected by S_{ij}^{A} close to 1 and S_{ij}^{B} close to 0.

In fact, a broad signal in a given map can overlap with more than one anomaly in the other map. This situation happens when the spatial resolution of the two compared gravity field models differs, leading to cases where two

neighboring signals are well resolved in one map but coalesce in the other. Hence, we redefine S to measure the fraction of the total amplitude of a signal A_i (resp. B_j), which is comprised in all its overlaps with the signals B_j (resp. A_i) of the other map:

$$S_i^A = \frac{\sum_{j=1}^{N_B} \int_{O_{ij}} \tilde{g}_{\mathcal{A}}(\theta,\phi)\mathrm{d}\sigma(\theta,\phi)}{\int_{A_i} \tilde{g}_{\mathcal{A}}(\theta,\phi)\mathrm{d}\sigma(\theta,\phi)} \tag{4}$$

$$S_j^B = \frac{\sum_{i=1}^{N_A} \int_{O_{ij}} \tilde{g}_{\mathcal{B}}(\theta,\phi)\mathrm{d}\sigma(\theta,\phi)}{\int_{B_j} \tilde{g}_{\mathcal{B}}(\theta,\phi)\mathrm{d}\sigma(\theta,\phi)} \tag{5}$$

The matrix K of entries k_{ij} summarizes the consistency in amplitude for all pairs of overlapping signals of similar sign in the two compared maps $\mathcal{A}$ and $\mathcal{B}$. The matrices S^A and S^B of entries S_{ij}^A and S_{ij}^B show the consistency in spatial extent for all these pairs. Summations over the columns of S^A (resp. over the lines of S^B) lead to the vectors S_A and S_B of entries S_i^A (resp. S_j^B) introduced in Equation 4 (resp. Equation 5), showing the consistency in spatial extent cumulated over all the pairs formed by each signal A_i (resp. B_j). Thus, by thresholding the entries of the matrix K and the vectors S_A and S_B, we can identify consistent signals between the two maps $\mathcal{A}$ and $\mathcal{B}$ at chosen levels of consistency.

Based on this procedure, we perform three types of consistency analyses between two gravity field models:

1. 1*Solutions Consistency*. Consistency between two different gravity solutions (GRGS03 and CSR06), with the same operation regarding their dealiasing ocean model: either removal or restoration. Here we test the robustness of each anomaly with respect to the GRACE data processing, and k provides the amplitude ratio between consistent signals in the two compared gravity field solutions.
2. *Ocean Model Consistency*. Consistency between two gravity solutions of the same group (either GRGS03 or CSR06), with and without restoration of the corresponding dealiasing ocean model. Here we test the sensitivity of each anomaly to the dealiasing ocean mass model; k provides the amplitude ratio between the contribution of this modeled source, and the sum of all the other contributions to the observed signal, including the noises (see Appendix B).
3. *Solutions and Ocean Model Consistency*. sequential application of the comparisons (1) and (2), to extract consistent signals between different GRACE gravity solutions, poorly impacted by their respective ocean models.

Figure 3b illustrates the principle of these comparisons. We first extract from each gravity solution the signals A_i, B_j which are not too sensitive to their respective dealiasing ocean model (*Ocean model consistency*). For each pair $\{k, S\}$ of threshold values for $|k|$, S_A, and S_B, these signals verify the three conditions: $|k_{ij}| < k$ and $S_i^A > S$ and $S_j^B > S$. Keeping the same threshold values $\{k, S\}$ and the same conditions, we select the consistent signals between two different GRACE gravity solutions (*Solutions consistency*) among those that have passed the previous selection. This sequence of tests, which order could be reversed, corresponds to the *Solutions and Ocean model consistency*. This way we identify robust signals across different gravity solutions, not much impacted by their respective dealiasing ocean models, with a chosen level of robustness as given by the $\{k, S\}$ thresholds. Unlike a direct averaging of different gravity field models, this approach preserves the specificity of each gravity field model while extracting its robust features from comparisons with the spatial structures of other models.

5. Application to the Signals Preceding the 2011 Tohoku Earthquake

We apply the methodologies described above to investigate whether the anomalous signal before the March 2011 Tohoku earthquake evidenced in Panet et al. (2018), can be automatically detected in the GRACE global gravity solutions as a specific feature originating from solid Earth. Thus, we focus on the orientation of the NorthWest Pacific subduction as previously mentioned. Without knowledge of the upcoming earthquake, all spatial scales should be systematically investigated. Here we show the results at intermediate spatial scales, 1,200–1,400 km, for which the most anomalous signal is detected; this signal progressively vanishes at smaller and at larger scales.

5.1. Anomalous Signals in the GRGS RL03 Gravity Solution

We first apply the optimal analysis to the GRGS03 gravity solutions and show the results at the 1,200-km scale, which provides an improved resolution of the signals along the direction of the subduction around Japan. In addition to numerous anomalies of lower magnitude, the February 2011 map of anomalous fast gravity gradient signals features only five areas of intense variations (Figure 4a): around North-Eastern Japan, in the North-West and the South-East of Australia, and in the Orenoco and the Amazon basins in South America. Around Japan, the gravity gradients exhibit an elongated dipolar structure, typical of dislocations along a fault plane (Figure 4c). This particular spatial structure, spreading across three different zones: the semi-enclosed Japan Sea, the Northern Japan islands and the open Pacific ocean, also remains after restoration of the dealiasing ocean model (Figures 4b and 4d). As discussed in Panet et al. (2018), such a feature does not coincide with the patterns and amplitudes of the water cycle signals in this region, documented from the variability of the seasonal and nonseasonal GRACE signals.

The robustness of this dipolar anomaly with respect to the ocean model correction is confirmed by the consistency analysis between the ocean-removed and ocean-restored GRGS03 gravity solutions. Most of the oceanic signals

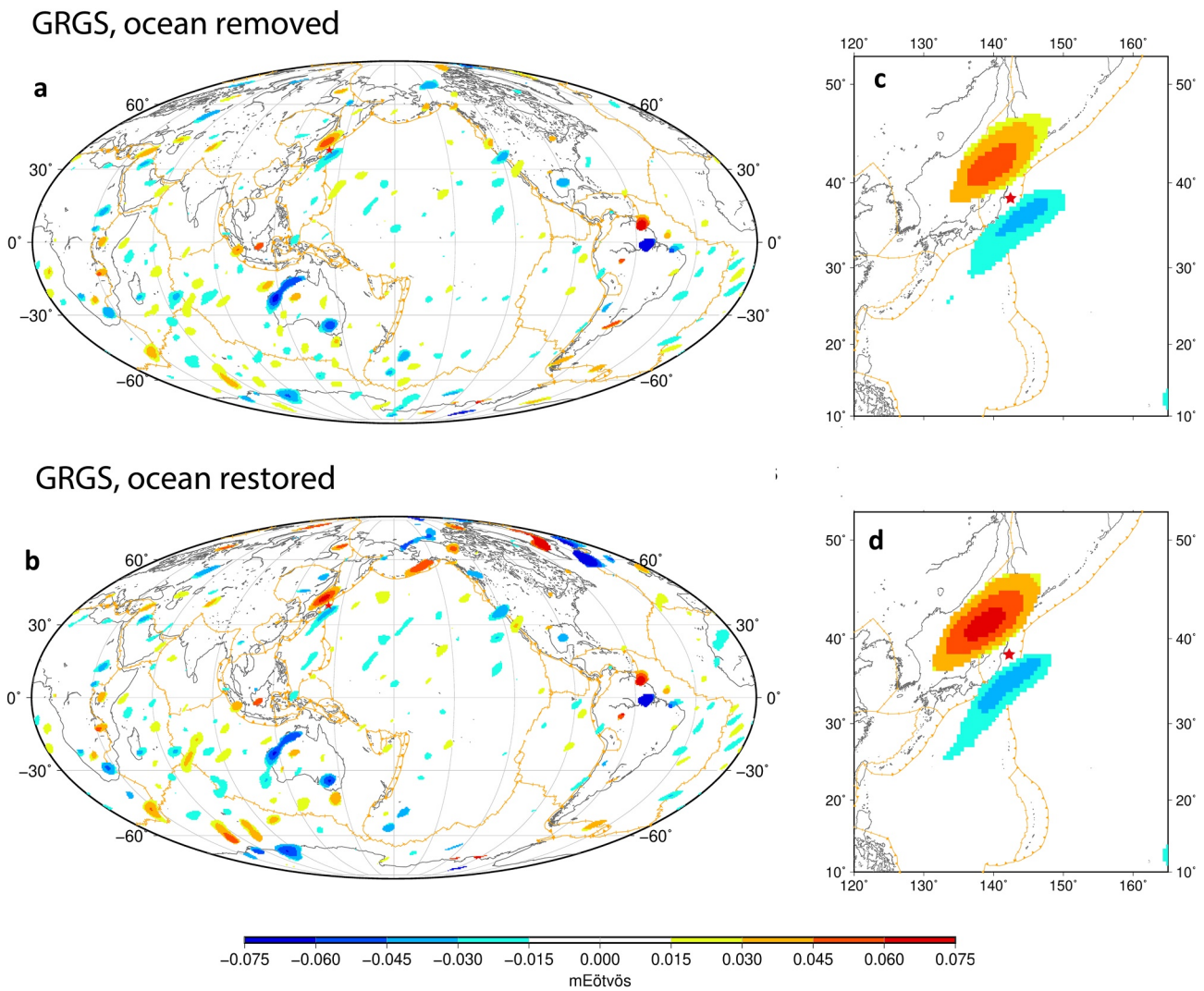

Figure 4. Anomalous signals in the optimal GRGS solution in February 2011. (a, b) Maps of the anomalous gravity gradient variations in the GRGS solution in February 2011 ($\phi\phi$ gradients at 1,200 km scale, *optimal* configuration), obtained as described in Section 3.2. The dealiasing ocean model has been removed from (resp. restored to) the GRGS geoids in panel a (resp. b). (c, d) Zooms around Japan of the maps shown in (a, b), respectively. Orange lines: plate boundaries (Bird, 2003), red star: epicenter of the 2011 Tohoku earthquake.

of smaller amplitude are strongly impacted by the ocean model and vanish for increasing S value and decreasing k value (Figure 5). On the contrary, the Tohoku positive and negative preseismic anomalies are associated to high S values (above 0.8) and low k values (below 0.25) (Figure 5, Figures 6a, 6d, and Appendix Figures C1a, C1d). Selecting the gravity gradient anomalies with a similar or better robustness to the dealiasing ocean model than these preseismic anomalies ($|k| \leq 0.26$ and $S \geq 0.8$) over the entire July 2004 to February 2011 time period before the earthquake, we then draw the distribution of the signal magnitudes all over the globe or only over the oceans (Figures 6b and 6e, Appendix Figures C1b and C1e). We find that the magnitudes of both the positive and the negative lobes of the Tohoku preseismic anomaly reach very high percentiles of these space-time distributions, above the 97.5% (resp. 99%) percentile for the positive lobe globally (resp. over the oceans), and above the 92% (resp. 99%) percentile for the negative lobe globally (resp. over the oceans). This conclusion remains valid when we vary the threshold values for k and S, in the range where the signal is preserved, as shown in Figures 6c, 6f and Appendix Figures C1c, C1f, C2a, and C2b for both the positive and the negative preseismic anomalies. Thus, the magnitude of the February 2011 short-term gravity gradient variations around Japan differs significantly from the usual variability of the gravity signals, which is dominated by the water cycle contributions. This difference is clear in space over the whole globe, and also in time. In addition, the anomalous gravity gradient variations exhibit a spatial structure typical of a solid Earth source, particularly well adapted to the geometry of the subduction zone on which it is observed, and robust with respect to the dealiasing ocean model. These results support the interpretation of Panet et al. (2018) as a preseismic signal at depth.

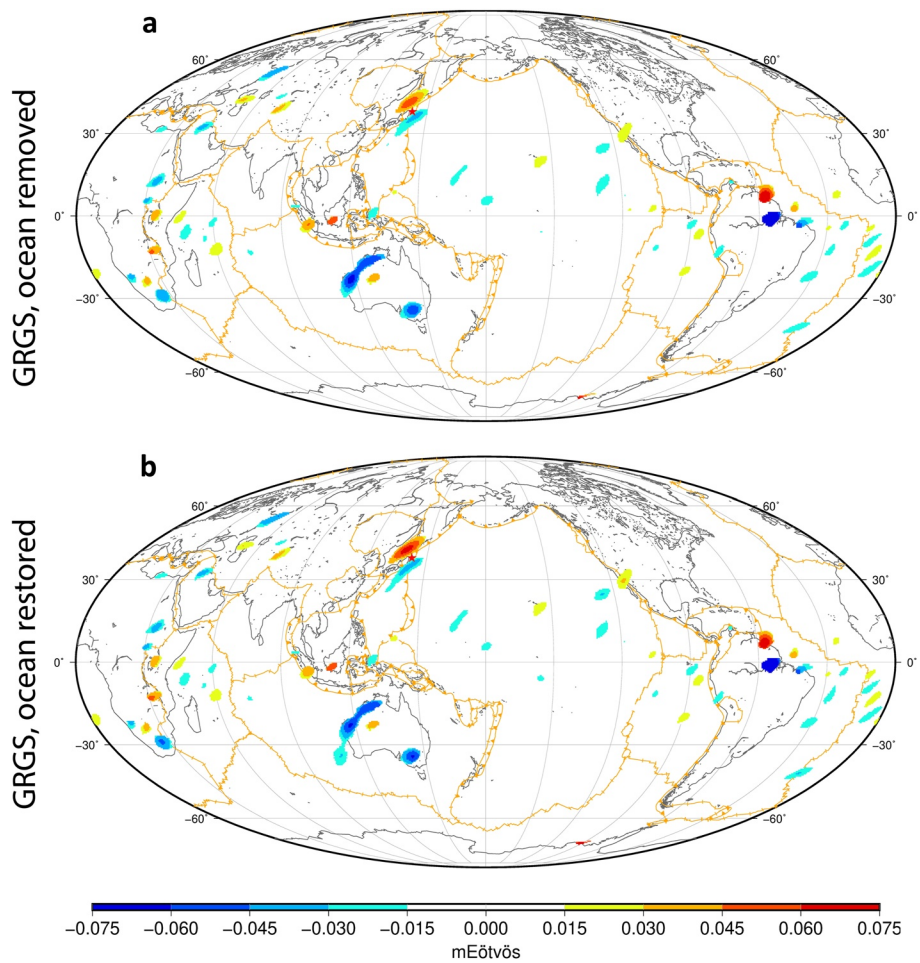

Figure 5. Signals selection in the optimal GRGS solution for February 2011, after testing the Ocean model consistency. Maps of the anomalous gravity gradient variations in the GRGS solution in February 2011 ($\phi\phi$ gradients at 1,200-km scale, *optimal* configuration), with (b) or without (a) restoration of the dealiasing ocean model. The maps show the selected signals for $|k| \leq 0.26$; $S \geq 0.8$ in the Ocean model consistency test, corresponding to a low sensitivity to the dealiasing ocean model.

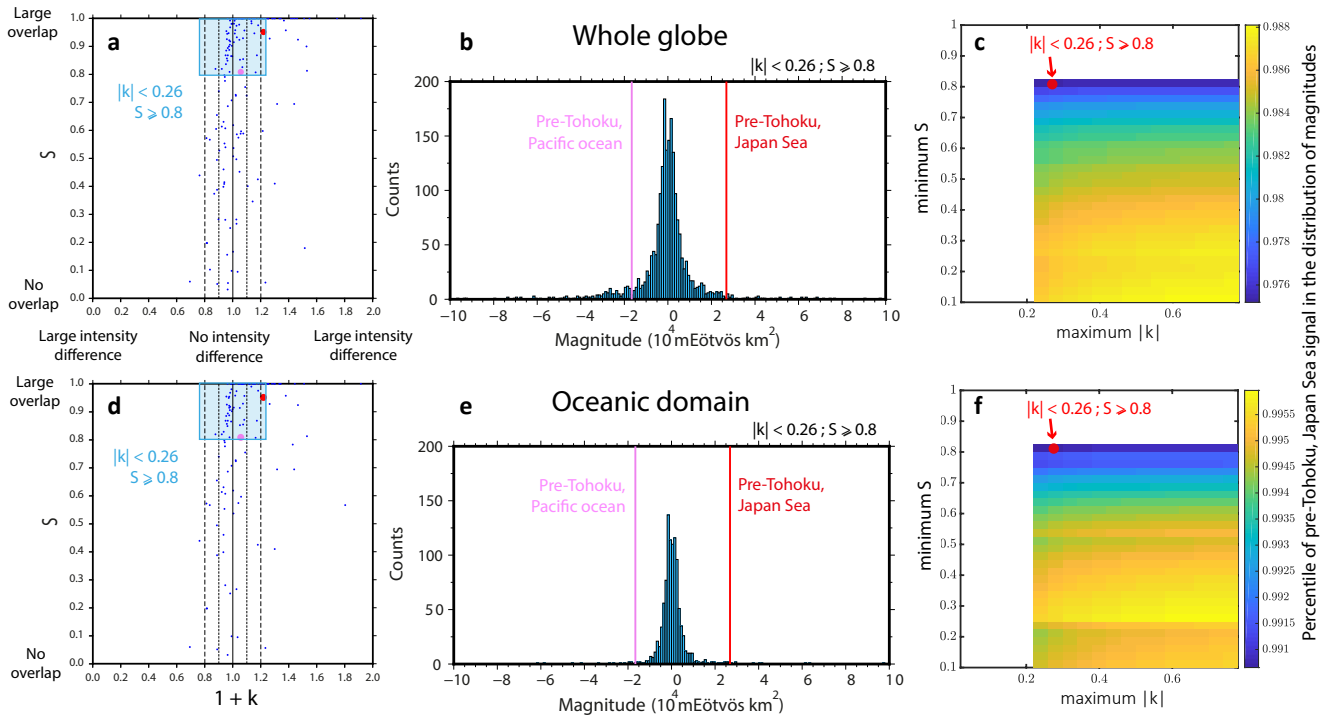

Figure 6. Space-time distributions of the signals magnitudes in the optimal GRGS solution, after testing the ocean model consistency. Anomalous signals from the 1,200-km scale $\phi\phi$ gravity gradients (GRGS solution, optimal analysis) over the July 2004 to February 2011 period, all over the globe (a–c) or over the ocean (d–f). (a, d) Values of the parameters k and S for each gravity gradient signal in the test of Ocean model consistency. Thick red point: values for the pre-Tohoku positive anomaly (Japan Sea) in February 2011; thick pink point: values for the pre-Tohoku negative anomaly (Pacific ocean); light blue box: values such that $|k| \leq 0.26$; $S \geq 0.8$. (b, e) Space-time distributions of the signals magnitudes for $|k| \leq 0.26$; $S \geq 0.8$. The magnitudes of the positive and negative February 2011 preseismic anomalies are indicated by the red and pink bars, respectively. (c, f) Percentile of the positive February 2011 preseismic anomaly in the Japan Sea in the space-time distributions of the signals magnitudes, as a function of the thresholds on $|k|$ and S. The top left corner corresponds to the extreme threshold values for $|k|$ and S which preserve the studied anomaly. Red dot: percentile obtained for $|k| \leq 0.26$; $S \geq 0.8$ (corresponding to the distributions shown in b, e). Note the very high percentiles whatever the thresholds for $|k|$ and S preserving the Japan Sea preseismic anomaly.

We have tested the consistency of the signal shown in Figure 4c with the preseismic gravity gradient anomalies presented in Panet et al. (2018). Part of the differences reflect the different spatial scales and orientations of the two analyses, or the different temporal resolutions in the case of Panet et al. (2018, Figure 1a). Even so, consistency tests indicate a good agreement with the positive lobe of the preseismic signal of the 2018 study (as shown in Supporting Information Figure S22, scale 1,200 km, $Az.$ 40°), with k values of ∼0.1 and S values of 0.95 and 0.75 for the newer and the older determinations of the signal, respectively. The amplitudes of the negative lobes are also found highly consistent ($k \sim 0.1$) while the S values reflect a broader extent of the newer negative anomaly ($S = 0.52$) compared to the older ($S = 0.96$). This difference corresponds to a better resolved dipolar structure across the Boso triple junction in the present study. Comparing the newer anomaly with the predictions of the normal faulting model used in Panet et al. (2018) as an equivalent representation for deep preseismic slab extension, we confirm the global agreement for a slightly increased amount of slip of 52-cm (Appendix E).

5.2. Comparison With the CSR RL06 Gravity Solution

5.2.1. Consistency Between the GRGS03 and the CSR06 Solutions

We then extend our analysis to the CSR06 gravity solutions. As explained in Section 3.1.2, only the degraded analysis can be carried out on these solutions, and we also apply it to the GRGS03 gravity solutions for comparison. Figures 7a–7d shows the anomalous fast gravity gradient signals in the Az_2 direction at the 1,400-km scale in February 2011. As could be expected, we obtain a larger number of signals in the degraded GRGS03 solution than in the optimal approach, due to the lower angular selectivity of the degraded analysis around an average 72.5°E direction, tilted with respect to the Japanese subduction. We then select the robust signals: not too impacted by the respective contributions of their ocean dealiasing models, and consistent in the GRGS and CSR gravity solutions

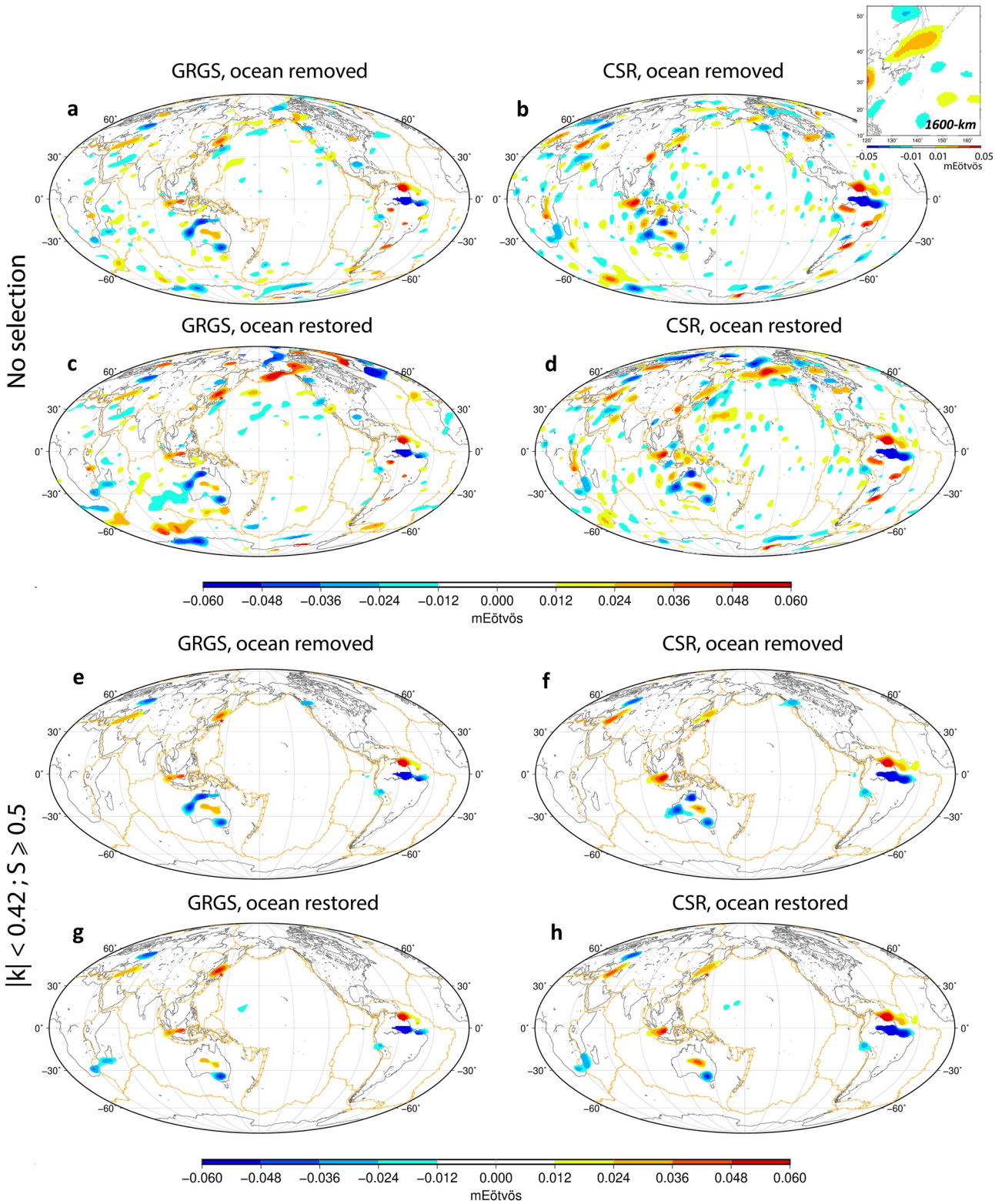

Figure 7. Anomalous signals and their selection after testing the Solutions and Ocean model consistency in the degraded GRGS and CSR solutions in February 2011. Maps of anomalous gravity gradient signals (1,400-km scale $\phi\phi$ gravity gradients, *degraded* configuration) in the GRGS and the CSR solutions in February 2011. (a–d) Original signals; (e–h) selected signals for an intermediate level of sensitivity to both the ocean dealiasing model and the GRACE solution in the test of Solutions and Ocean model consistency ($|k| \leq 0.42$; $S \geq 0.5$).

(*Solution and ocean model consistency*). Figures 7e–7h show the remaining signals for intermediate {k, S} values in February 2011. They include the positive lobe of the Tohoku preseismic anomaly (well resolved at the larger 1,600-km scale as shown in the inset map of panel b), as well as a few large signals over major river basins (Orenoco, Amazon, Murray-Darling, Volga), across the Caspian Sea, in the North and West of Australia and over Indonesia. Note that the negative lobe of the Tohoku preseismic anomaly is not selected due to its smaller amplitude in the CSR solution. Among the anomalies common to the two fields, the gravity gradient increase in the Japan Sea before the Tohoku earthquake is one of the most consistent signals between the CSR and the GRGS gravity solutions in February 2011. Increasing the S value up to 0.8, it is one of the only three anomalies left during that month (Figure 8), with the Volga and the Murray-Darling anomalies. Thus, it is detected with an extremely high consistency between both the CSR and the GRGS gravity solutions, independently from their respective oceanic corrections. Major signals over the Amazon basin do not show such a high consistency between the two gravity solutions. As expected for hydrological sources involving different river systems (Blöschl & Sivapalan, 1995), they may result from mass redistributions over a broad range of spatial and temporal scales. These complex signals combining large gravity variations over a range of scales could be more sensitive to differences in spatial resolutions between the two solutions, and/or to the strategies applied to minimize the striping artifacts (i.e., the regularization in the GRGS solution vs. the DDK filtering of the CSR solution).

5.2.2. Investigation of Possible Hydrological Sources

Except around Japan, most signals identified in Figures 7e–7h can be related to well documented, large water mass redistributions concomitant with the shift from the 2009/2010 El Niño event to an intense 2010/2011 La Niña episode, the strongest over eight decades (Boening et al., 2012). Starting in mid-2010, it was marked by a decline in the ocean mass and a corresponding increase in the continental water storage, in particular over Australia and Indonesia, over South-East Asia and northern South America (Boening et al., 2012; Fasullo et al., 2013). Both El Niño and La Niña events have been associated with extreme climatic conditions in different areas of the world, including intense rainfalls and floods in the Murray-Darling basin and across Australia (Trenberth & Fasullo, 2012) after years of drought there (van Dijk et al., 2013). Heavy precipitations during a tropical cyclone have been recorded in the North of Australia in February 2011, while the West of Australia experienced flooding from December 2010 to February 2011 (Waddell et al., 2012). Over the central Amazon basin, the large fluctuations in the gravity gradients time series coincide with an intensification of extreme hydro-meteorological conditions over the last decade (e.g., Gloor et al., 2013). An exceptional flood occurred in 2009 and was detected from GRACE consistently with precipitation data (Chen et al., 2010), preceding a major drought in 2010. The February 2011 negative gravity gradient anomaly reflects the recovery from this drought, which corresponds to an increase in water storage. In addition, we have verified that the positive anomaly to the North could be a related edge effect. Over Indonesia, the positive gravity gradient anomalies coincide with the recovery from the Fall 2010 flooding, thus water mass decrease. Over continental Europe, the negative gravity gradient signal in the Volga basin is consistent with water mass increase after the Summer 2010 heat wave and wildfires in Russia (Trenberth & Fasullo, 2012). To the South, we have verified that the positive anomaly actually results from the coalescence of two anomalies, over the Caspian Sea and in Turkey. Over the Caspian Sea, it reflects a steady increase in the gravity gradients, thus mass decrease, reminiscent of the long-term sea level drop there (Chen et al., 2017). Such large trend is indeed not removed in our constant extrapolation of the lower temporal frequencies in the end of the time series. We finally notice that this consistency between the location and sign of the gravity gradient anomalies and those of the large water mass redistributions concomitant with the 2010/2011 La Niña event, is not valid around Japan. There, La Niña events are often associated with increased winter precipitations due to a combination of atmospheric moisture and cold winds (Ueda et al., 2015, 2017), inconsistent with the observed gravity gradient increase and mass decrease signal.

5.2.3. Temporal Uniqueness of the Selected Signals

Among all the largest anomalies, the unusual character of the Tohoku positive preseismic signal is further illustrated by investigating the temporal frequency of occurrence of anomalous signals. It is described in Figure 9, showing that the signals are preferentially located over continental hydrological systems for the investigated July 2004 to January 2011 period. For instance, a number of anomalous variations are recorded in the Orenoco and in the Amazon basins, over broad regions in Australia, around Indonesia or in the Volga basin. In contrast, only one gravity gradient anomaly is detected around Japan and two across the border with Corea in the CSR solution, over the considered time period. No anomaly is recorded in the GRGS solution.

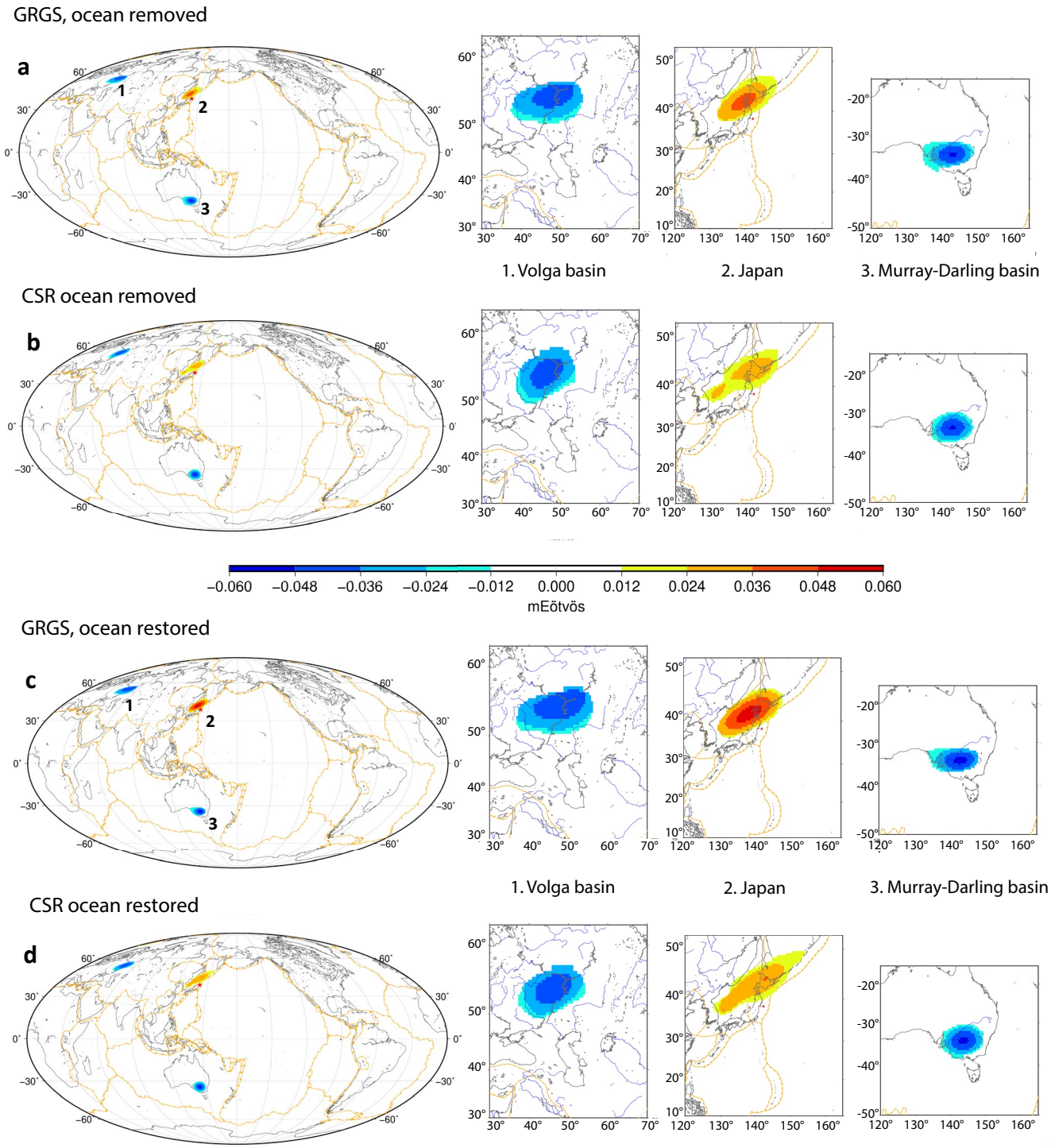

Figure 8. Most consistent signals in the degraded GRGS and CSR solutions in February 2011. Same as Figure 7, for a lower level of sensitivity to both the ocean dealiasing model and the GRACE solution and for all gravity models, with or without restoration of the ocean model (GRGS solutions in (a, c) $|k| \leq 0.34$; $S \geq 0.8$; CSR solutions in (b, d) $|k| \leq 0.42$; $S \geq 0.8$). Zooms in the areas of the three remaining signals (Volga and Murray-Darling drainage basins, Japan Sea) are shown in the right inset maps.

Finally, we have investigated the temporal uniqueness of the Tohoku positive preseismic anomaly all over the globe and over the whole oceanic domain. We analyze the GRGS or CSR gravity solutions independently from each other, to test the sensitivity of the signals to the respective ocean dealiasing models (test of *Ocean model consistency*). Whatever the threshold on $|k|$ and S in the range preserving the Tohoku positive preseismic anomaly,

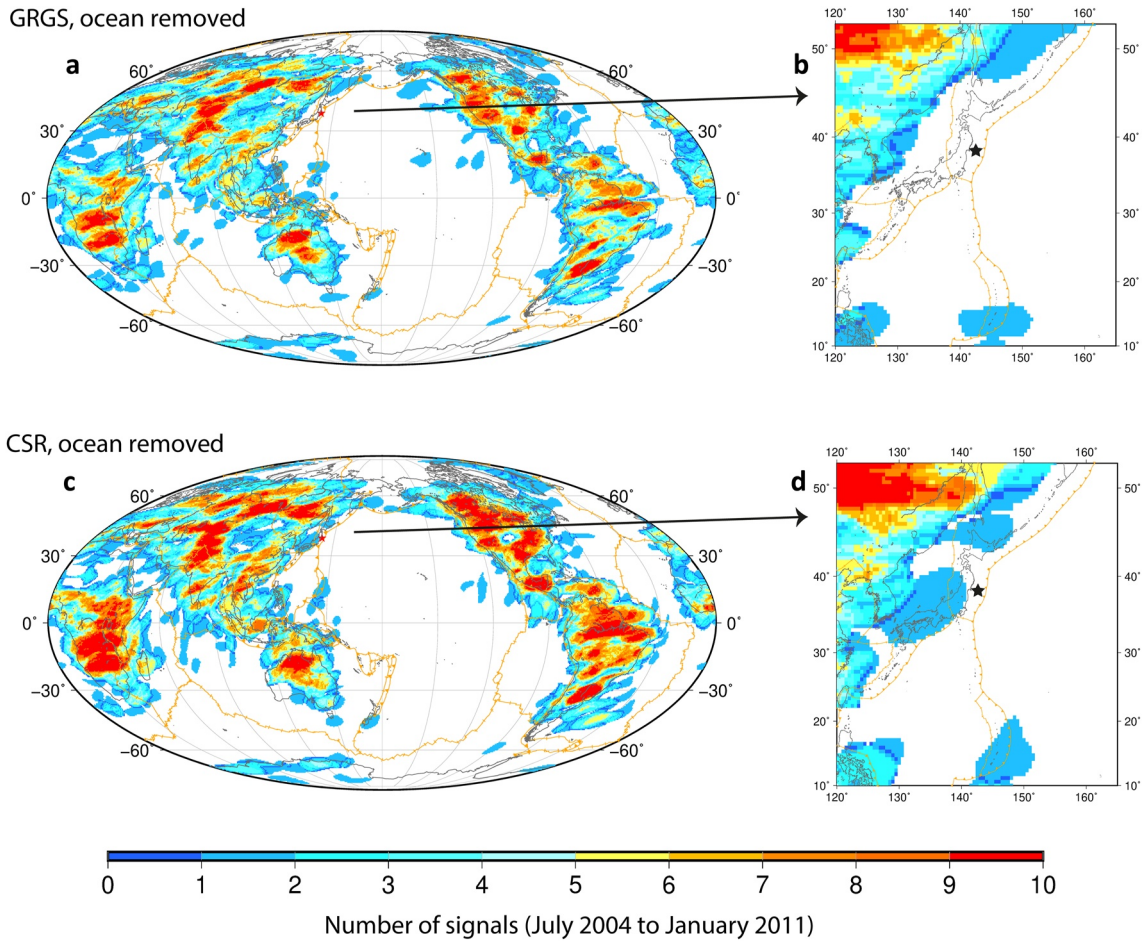

Figure 9. Localization of the selected signals in the degraded GRGS and CSR solutions. Map showing at each point the number of anomalous signals over the July 2004 to January 2011 period overlapping this point (1,400-km scale $\phi\phi$ gravity gradients, degraded GRGS and CSR solutions) in the degraded GRGS (a, b) and CSR (c, d) solutions, for the same thresholds in the test of Solutions and Ocean model consistency as in Figure 7 ($|k| \leq 0.42$; $S \geq 0.5$). Note the absence of such signals around Japan in the GRGS solution, and only one signal in the CSR solution.

we find that the magnitude of the pre-Tohoku signal exceeds the 95.5% percentile of the space-time distributions over the oceans, and the 91% percentile of the space-time distributions all over the globe (Figure 10b, 10c, Appendix Figure C3). This indicates a highly anomalous signal in each gravity solution, globally in space and time. These percentiles degrade when considering the distributions obtained in the joint analysis of the CSR and GRGS solutions (test of *Solutions and Ocean model consistency*). Indeed, this analysis preferentially selects large continental hydrology and coastal signals, more consistent between the CSR and the GRGS solutions than the open ocean anomalies. In particular, the selected coastal signals are large because they are often associated with nearby continental hydrology sources, as in the case of continental signals leaking across the coast. This is not the case of the February 2011 Tohoku anomaly, as shown in Panet et al. (2018) and in Appendix D, and as also underlined by the absence of corresponding continental signals in Figures 4, 5, and 7.

6. Discussion

We have shown in the GRACE data the robust and anomalous character of the gravity gradient variations around Japan prior to the March 2011 Tohoku earthquake, without any hypothesis on the consecutive behavior of the time series. This signal appears nearly unique, contradicting the results of Wang and Bürgmann (2019), who also address the question of the global detection of the anomalous gravity gradient signal before the Tohoku earthquake. This is due to the fact that the two analyses are based upon different steps (Section 6.1). In addition, the question of uniqueness can only be discussed by taking into account the specific characteristics of the gravity signals generated at depth along subduction zones (Section 6.2).

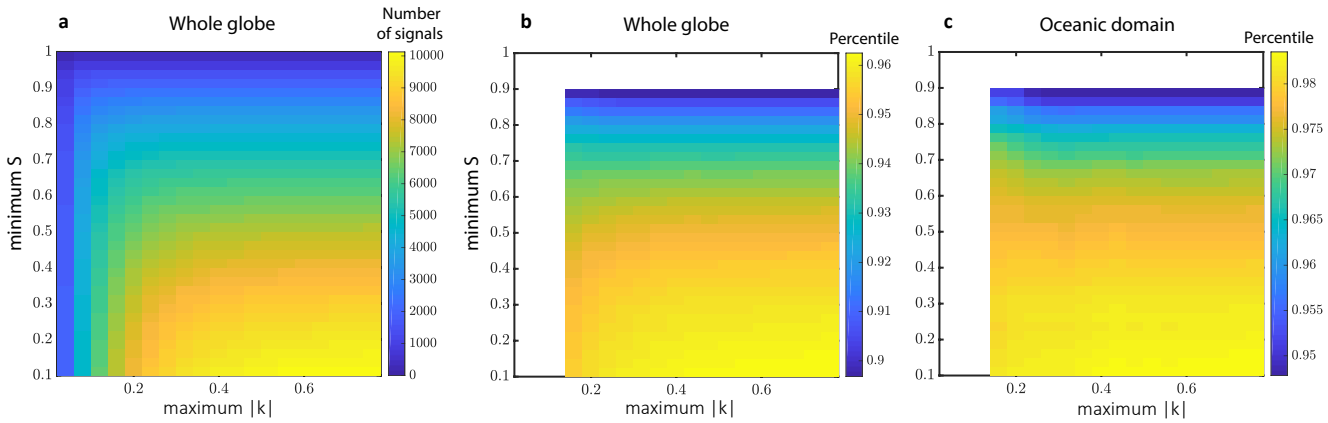

Figure 10. Singularity of the positive February 2011 preseismic anomaly in space and time in the CSR06 gravity solution, after testing the ocean model consistency. (a) Number of selected signals in the test of Ocean model consistency over the period from July 2004 to February 2011, as a function of the thresholds on |*k*| and *S*. (b, resp. c) Percentile of the positive February 2011 preseismic anomaly in the space-time distributions of the magnitudes of the anomalous signals over the same period, as a function of the thresholds on |*k*| and *S*, considering the signals all over the globe (resp. in the oceanic domain). Note the high percentile of the Tohoku preseismic anomaly whatever the thresholds for |*k*| and *S* preserving this anomaly. All panels correspond to the 1,400-km scale $\phi\phi$ gravity gradients, degraded CSR solutions with the dealiasing ocean model removed.

6.1. Methodological Comparison With the Study of Wang and Bürgmann (2019)

Wang and Bürgmann (2019) test at each spatial point whether there is a significant break in slope of the gravity gradients between the long-term behavior and the four or 8 month period preceding the 2011 Tohoku earthquake. Because the preseismic change in trend appears statistically nonunique, in space and in time, the authors conclude that this signal is not fundamentally different from the predominant contributions of the water cycle and from the noises, and thus cannot be significantly attributed to a solid Earth deformation process. The analysis we conduct here differs in many ways, as detailed below:

1. *Data Processing*. We have applied a DDK6 filter as a post-processing step of the CSR06 solution. Compared to the more conservative truncation at the spherical harmonics degree/order 40 used in Wang and Bürgmann (2019), we enhance the spatial resolution of the CSR06 gravity field model while minimizing the GRACE striping artifacts.
2. *Definition of the Multiscale Gravity Gradients.* We apply the spherical wavelet filters *before* computing the gravity gradients and not *afterward* as described by Wang and Bürgmann (2019). This difference is crucial, because all the components of the gravity gradient tensor may not correspond to the same mass source in the latter case, contrary to the former case, as shown in Panet (2018, Appendix A).
3. *Investigated Orientations*. In our study, the gravity gradients are computed in the Az_2 azimuth range, or from the combination of the Az_1 and Az_2 ranges in the optimal approach. Compared to the Az_1 azimuth range used in Wang and Bürgmann (2019), we obtain a lower sensitivity to the GRACE striping noise, especially for the CSR06 gravity field models. In our *optimal* approach and the GRGS solutions, we obtain an improved angular resolution on the orientation of the considered plate boundary.
4. *Temporal Analysis*. To extract anomalous preseismic behaviors, Wang and Bürgmann (2019) test if the linear trend of the gravity gradient time series estimated over long times exhibits a significant change during the few months before the earthquake. This temporal model is incomplete in many areas such as hydrological basins, where water storage variations are expected to occur over a wide range of temporal scales (Blöschl & Sivapalan, 1995) and where the amplitude of the seasonal cycle may vary. Hydrological parameters show a significant level of non-Gaussianity, and so do the GRACE gravity time series (see Forootan & Kusche, 2012, and references therein). In such areas, without taking these temporal correlations into account, the detected transient changes in trends may be part of the natural variability but add numerous signals in the anomaly maps. Here, such contributions are minimized using a sliding window algorithm that removes the low temporal frequencies from the time series and focuses on the short timescale residuals. This way, we better take into account the spatially heterogeneous behavior of the time series, and improve the identification of anomalous short-term changes considering a Gaussian white noise model.

5. *Amplitude of the Signals*. We consider the absolute magnitude of the gravity gradient signals, to compare the anomalies obtained over different areas and to assess the robustness of the signals. Without such an ingredient, smaller contributions are equally selected in Wang and Bürgmann (2019).

All these differences in data processing and methodologies for the analysis of gravity field models explain the different results of the two studies based on the same GRACE gravity solutions. Both studies seek to identify an anomalous, preseismic signal based on a specific signature in the GRACE data, without introducing prior models. Here, we further assess its robustness with respect to errors in the GRACE gravity solutions using the consistency analysis. Such errors can result in particular from the use of imperfect background models in the dealiasing of the observations and from the chosen inversion approach. Our methodology also differs from that of Chao and Liau (2019), who perform an Empirical Orthogonal Functions analysis to objectively extract earthquake-induced spatiotemporal variations of the gravity field. Their approach does not capture the pre-Tohoku signal, probably because it is applied on the full space-time gravity signal rather than individual variations at specific spatial and temporal scales, along a preferred orientation. Part of the differences may also come from improvements between the CSR Release 5 and 6 solutions.

6.2. Identification of Deep Slab Signals Along Subduction Boundaries

The gravity gradient variations around Japan before the Tohoku earthquake appear singular, not only because of their size and consistency in different gravity field models (Section 5), but also because our analysis reveals that they have all the characteristics of gravimetric signals induced by dislocations at depth along a subducting slab. As discussed above (Section 6.1), this is made possible by a better separation of the short timescales, a reduced sensitivity to the striping noise and a closer focus on the orientation of the Northwestern Pacific subduction in the optimal approach. Actually, the interpretation of the signals in terms of dislocation at depth is guided by their specific signature, made of a dipolar spatial pattern across sea, islands and ocean around Japan. Such pattern differs from usual fingerprints of water cycle and noise (Panet et al., 2018). This difference reinforces the singularity of the preseismic signal, more than the absence of other gravity variations. The same reasoning can also be applied to the co-seismic gravity gradient variation, which may seem nonunique compared to other mass redistributions within the Earth system in March 2011 (Wang & Bürgmann, 2019), but which becomes unequivocal when considering its geometry and amplitude, along the Japanese subduction.

As shown by Panet et al. (2018, Supporting Information Section 3.3.2), the close focus on the orientation of the studied subduction boundary also isolates the subduction-aligned preseismic signal from hydrological sources of Eastern Asia. Combined with investigations of a broader range of spatial scales, we have highlighted different spatial structures for the positive preseismic anomaly in the Japan Sea as compared to the negative signals over Eastern China in February 2011 (see Appendix D). These differences reveal independent sources, which could not be resolved from each other in the analysis of Wang and Bürgmann (2019). For gravity solutions with a higher level of striping artifacts in the North-South oriented gradients, the reduction of the applied geometrical constraint in the degraded analysis and the coarser spatial resolution make it more difficult to decipher solid Earth dislocation sources from water resource variations using the shape and precise orientation of their gravitational signal. In addition, it naturally leads to a higher number of signals.

As compared to the present example of the 2011 Tohoku earthquake, the discussed singularity may be more difficult to identify for solid Earth sources of smaller magnitudes. In this case, comparisons with the location and amplitudes of the signals predicted by prior models of candidate sources, for instance using the methods introduced in this work, are more appropriate in order to decipher the origin of the observed gravity variations. For instance, comparisons based on hydrological models and in situ observations have made possible to identify deep preseismic gravity signals for the 2010 Maule earthquake, likely to result from sudden slab motion near 150-km depth (Bouih et al., 2022). Carried out in a systematic way using the consistency analysis we present here (Section 4), such comparisons could highlight singular signals in the GRACE data. Once again, this singularity would be based on the agreement between geophysical models and the GRACE signal, and would not result from the absence of any other mass redistributions within the Earth fluid envelope at the investigated spatial and temporal scales (Wang & Bürgmann, 2019). We finally note that comparisons between the observed satellite gravity gradient signals and those predicted from an ensemble of water circulation models could also provide a useful evaluation of these models.

Beyond the case of the 2011 Tohoku earthquake, these methods can be further developed in order to monitor deep mass redistributions along the Pacific subduction belt, potentially related to slab motions. It requires an adjustment of the spherical frame orientation to the local directions of the circum-Pacific subduction boundaries, and a systematic investigation of a range of spatial scales. Then, consistency tests can be performed based on global water circulation models, complemented where it is possible by regional hydrological and oceanic models. In areas where the accuracy of these models is questioned, the next step is to take advantage of the spatial or the temporal structure of the water sources that could be obtained from the geographical boundaries of the drainage basins or from time series of in situ observations. Independently of these developments, the temporal analysis of the gravity gradients we present here is carried out without knowledge of the rupture. Calling for sustained observations of time-varying gravity from satellites, this methodology can thus be applied either retrospectively after an earthquake, or for continuous monitoring of subduction zones in real time.

7. Conclusion

Our analysis shows that we can detect before a giant earthquake anomalous gravity gradient variations along a subduction boundary, likely to reflect processes related to internal deformations or discrete dislocations within the slabs at depth. It confirms the preseismic nature of the gravity gradient variations before the 2011 Tohoku earthquake, previously proposed from a study of the signal in its local context. Computing the gravity gradients along the respective orientations of each section of the Pacific subduction belt and at different spatial scales, our methodology can be further developed in order to systematically investigate a wide range of gravitational anomalies related to slab motion at depth, and document the dynamics of the most hidden component of this plate boundary and its interactions with deep and shallow seismic events. With a unique sensitivity to mass redistributions at depth in the subduction system and a global coverage, satellite gravity may thus provide a monitoring of subduction zones all over the globe at intermediate timescales, complementary to the observations of seismicity and to the space-geodetic determinations of upper plate deformations. It has the potential to detect transient motions deep in the subducted slab, corresponding to regional-scale changes in the slab pull force, before the occurrence of shallower deformation transients and foreshocks that would result from their propagation toward the surface. This could be an important contribution to alert systems in highly seismic zones, as also shown in Bouih et al. (2022) for the 2010 Maule earthquake. At the same time, the joint modeling of seismic, geodetic and time-varying gravity data can provide new information on the three-dimensional rheological structure and short-term dynamics of subduction zones.

Appendix A: Extrapolation Error of the Smoothed Time Series in February 2011

Here we evaluate the error in the estimation of the short-term residuals in February 2011 due to neglecting the smoothed variations of the gravity gradient time series over the last $N/2$-month interval of the time series truncated in February 2011: [February 2011—$N/2$ months; February 2011]. N is the width of the running window used to build the smoothed time series (denoted $\hat{g}_N$) from the observed gravity gradients (denoted g) and to derive the short timescale residuals by the difference: $\tilde{g}_N = g - \hat{g}_N$. For a given choice of N, we consider all the $N/2$-month long segments of the smoothed time series over the timespan T from 2004 to March 2010. We assume that the differences between the starting and ending values of these segments ($\hat{g}_N(t_i) - \hat{g}_N(t_i - N/2\,months)$ for t_i in T) follow a Gaussian distribution of mean μ and standard deviation σ, and compute the (μ, σ) parameters. This way we can estimate the probability for the difference $\tilde{g}_N(t_{end}) = g(t_{end}) - \hat{g}_N(t_{end}) = g(t_{end}) - \hat{g}_N(t_{end} - N/2\,months)$, with t_{end} = February 2011, to be entirely explained by the smooth variations which have been neglected in the constant extrapolation of $\hat{g}_N$ between $t_{end} - N/2\,months$ and t_{end}. It is indeed given by the percentile of $\tilde{g}_N(t_{end})$ in the distribution $\mathcal{N}(\mu, \sigma)$. This percentile is a function of the standardized anomaly $\tilde{G}_N(t_{end}) = \frac{\tilde{g}_N(t_{end}) - \mu}{\sigma}$.

We have computed the average of the standardized anomalies $\tilde{G}_6$ and $\tilde{G}_{12}$ in February 2011 for the different configurations of analysis of the GRACE gravity gradients. Over the oceans, the probability for the February 2011 residual signal $\tilde{g}_N(t_{end})$ to result from an error of extrapolation of the smooth variations is small, as could be expected. This reflects the low variability of the GRACE gravity data at seasonal to interannual timescales in these regions. In contrast, this variability increases over the continental hydrological systems, leading to larger risks of extrapolation errors over the continents. In the case of the February 2011 gravity gradient signals around Japan, the extrapolation error is likely very low in the GRGS gravity field (with a standardized anomaly above 4.5 in absolute value for both the optimal and the degraded analyses). In the CSR gravity solutions (degraded

analysis), the standardized residuals exceed 4 around Northern Japan (latitudes >40°N), and 3 in the Japan Sea, indicating a still limited level of error there.

Appendix B: Sensitivity of a Gravity Solution to the Ocean Dealiasing Model

Let us detail the example of a comparison of two GRACE solutions of the same group, with or without restoration of the ocean dealiasing model (test of Ocean model consistency). We use the following notations:

$$g_A = g_{\text{oc model}} + g_{\text{other sources}} + \epsilon_{\text{oc model}} + \epsilon_g \tag{B1}$$

$$g_B = g_A - g_{\text{oc model}} \tag{B2}$$

where g_A (resp. g_B) is the GRACE gravity gradient in the map A (resp. B), $g_{\text{oc model}}$ is the gravity gradient predicted from the ocean model, $g_{\text{other sources}}$ is the gravity gradient associated with the other mass sources within the Earth system, $\epsilon_{\text{oc model}}$ is the contribution of the mismodeled ocean sources and ϵ_g the errors of the considered gravity field model (here GRGS03 or CSR06), expressed in terms of gravity gradients. Because a seasonal cycle has been removed in the first steps of the postprocessing, all these terms correspond to the nonseasonal variabilities. We have:

$$k = \frac{g_{\text{oc model}}}{g_{\text{other sources}} + \epsilon_{\text{oc model}+\epsilon_g}} \tag{B3}$$

where the values $g_{\text{oc model}}$, $g_{\text{other sources}}$, $\epsilon_{\text{oc model}}$, and ϵ_g are integrated over the considered overlap.

Appendix C: Singularity of the Positive February 2011 Preseismic Anomaly in Space and Time in the GRGS Gravity Solution, After Testing the Ocean Model Consistency

Figures C1, C2 and C3. Here we show complements to Main Figures 6 and 10. We assess the singularity of the positive pre-Tohoku anomaly in the GRGS, ocean restored solutions, and of the negative pre-Tohoku anomaly in the GRGS standard solutions (optimal analyses, complement to Main Figure 6). We also assess the singularity of the positive pre-Tohoky anomaly in the GRGS standard solutions, for the degraded analysis (complement to Main Figure 10).

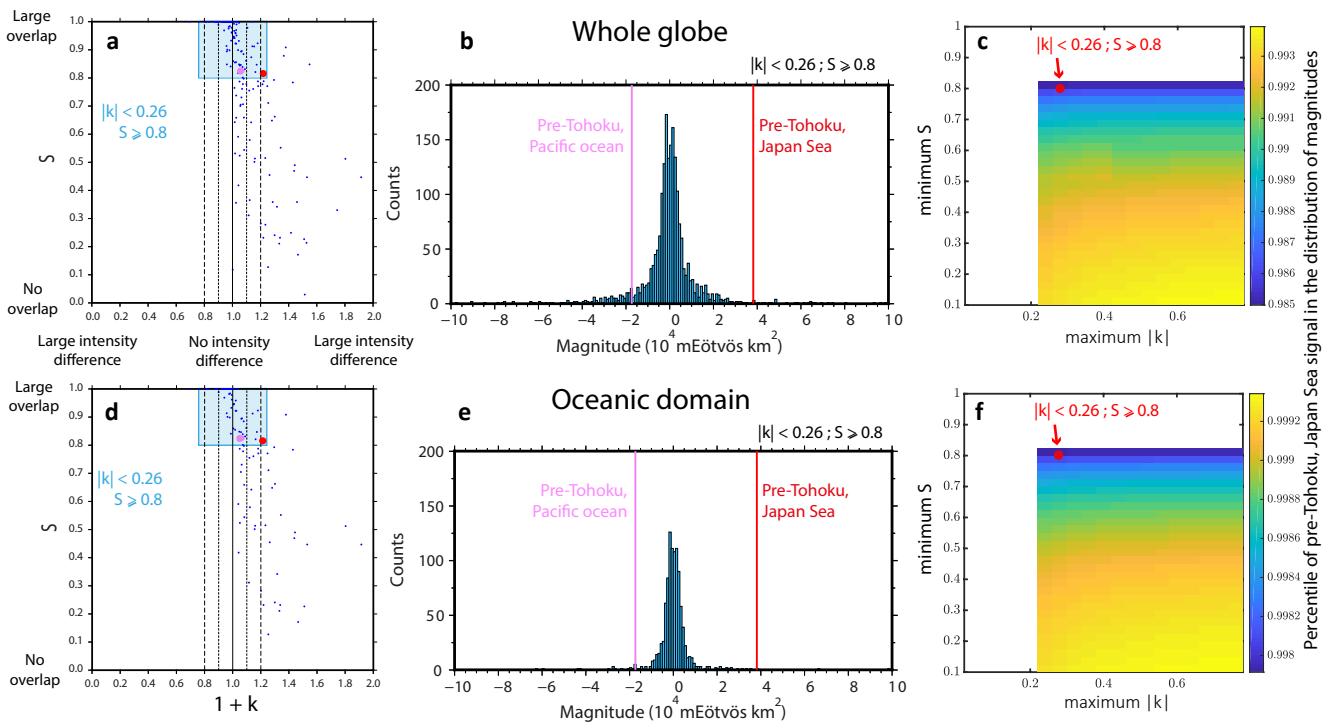

Figure C1. Same as Main Figure 6, with the ocean dealiasing model restored to the optimal GRGS solution.

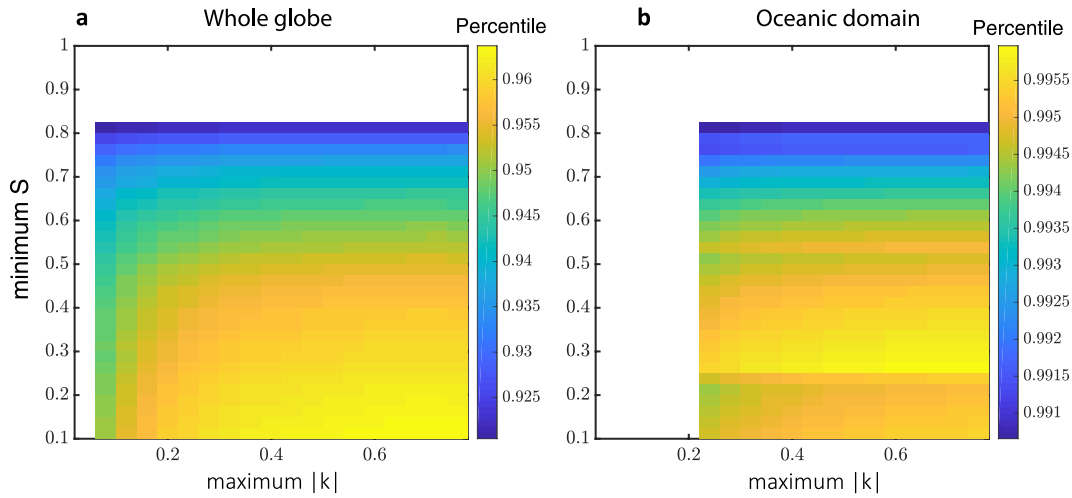

Figure C2. Same as Main Figure 6c and 6f, for the negative lobe of the February 2011 Tohoku preseismic anomaly.

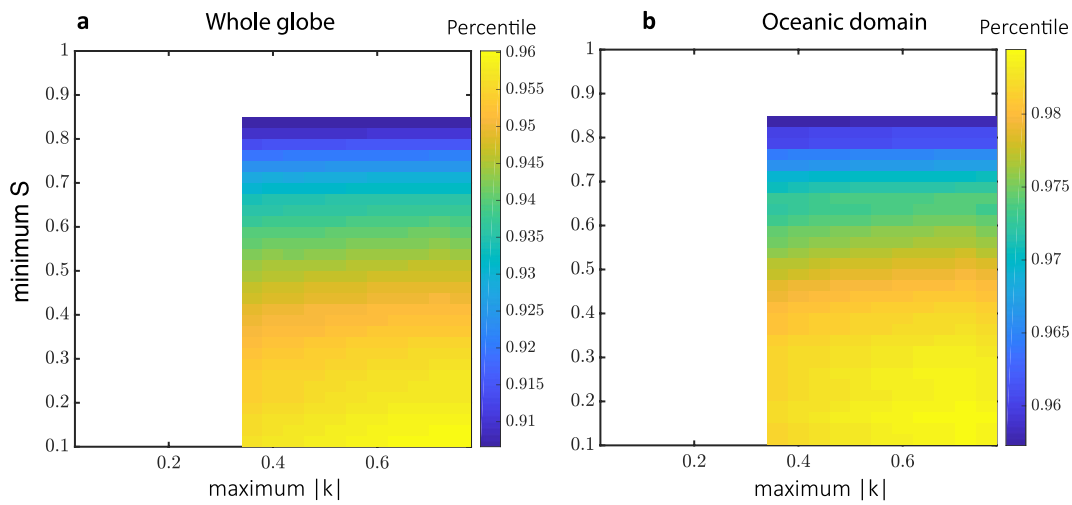

Figure C3. Same as Main Figure 10b and 10c, for the degraded GRGS solution (dealiasing ocean model removed).

Appendix D: Separation of the Tohoku Preseismic Signal From the Continental Signals

Gravity gradient time series corrected only from a long-term trend and from annual, semiannual, and 161-day sinusoidal cycles exhibit a large negative signal over Eastern China (Figure D1a), commented by Wang and Bürgmann (2019) and studied by Panet et al. (2018, Supporting Information Section 3.3.2 and Figure S27). The geometry of this anomaly is not fully described when considering only the 1,400-km scale and the Az_1 orientations, as done in Wang and Bürgmann (2019), leaving ambiguities on a possible connection with the positive preseismic anomaly in the Japan Sea. However, a better spatial characterization of this signal can be obtained by investigating a broader range of spatial scales to increase the resolution, and by applying the "*optimal analysis*" to the 1,000-km scale gravity gradients. This way, we have shown that the positive Japan Sea anomaly remains nearly unchanged in both the Az_1 and Az_2 directions, with a structure similar to that obtained at the 1,400-km scale (Figures D1a, D1c, and D1d). In contrast, the negative anomaly over the continent results from the coalescence of two smaller sources. These two sources coalesce in the Az_1 direction of their alignment (Figure D1c), but they are separated in the Az_2 direction and thus, in the optimal analysis (Figures D1d and D1e). Because of these different spatial structures, we noticed that the Japan Sea anomaly could not be a side effect of this continental anomaly and must be instead an independent signal. This conclusion was confirmed by finding similar negative anomalies over Eastern China in August 2010, without any related anomaly in the Japan Sea. It is also confirmed by an investigation of the time series in the negative China anomaly in February 2011 (Figure D1b). A symmetrical behavior with respect to the fast increase of the gravity gradients in the Japan Sea at the beginning of 2011 would involve a large decrease between December 2010 and February 2011 over China, which is not observed.

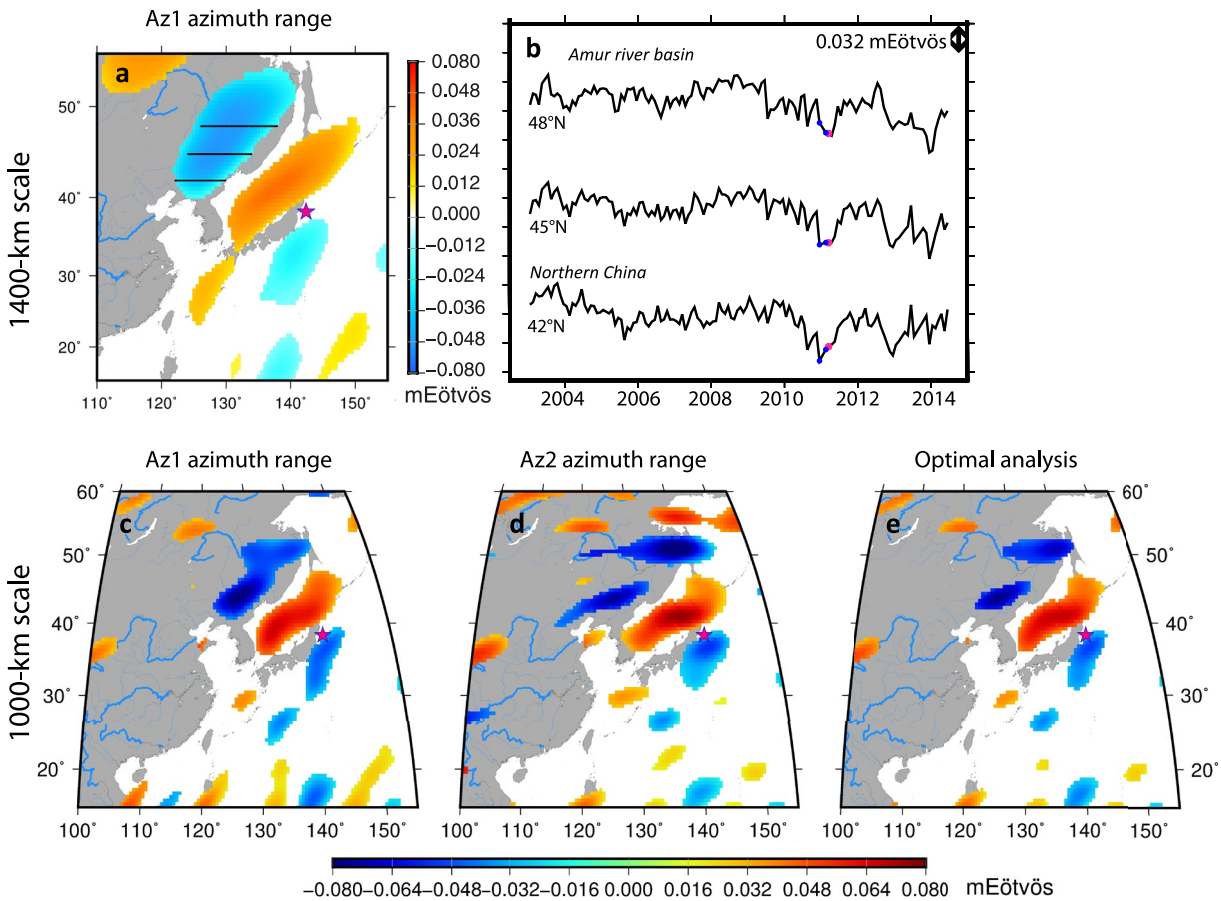

Figure D1. (a, b) 1,400-km scale $\phi\phi$ gravity gradients, Az_1 azimuth range, GRGS03 solutions (ocean model removed). (a) Map of anomalous signals (outside the [2.5–97.5%] percentile range of the long-term distribution) in February 2011; (b) time series stacked in longitude along lines of constant latitude across the negative China anomaly, marked by the black lines in (a). Blue dots: values in December 2010 and February 2011, pink dot: March 2011. (c–e) Maps of anomalous signals (outside the [5–95%] percentile range of the long-term distribution) of the 1,000-km scale $\phi\phi$ gravity gradients in February 2011 (same gravity solution). (c, resp. d): anomalies obtained for the azimuth range Az_1 (resp. Az_2; (e) anomalies obtained in the optimal analysis.

Appendix E: Deep Preseismic Normal Faulting Model

We calculated the preseismic signal predicted by the normal faulting model used in Panet et al. (2018, Supporting Information Section 6.2.1) to represent deep slab extension, for comparison with the GRACE anomalies shown in Main Figure 4c. This model corresponds to 40-cm slip along a 100-km wide, 1200-km long, 60° dipping, 230°N striking plane between the depths 245 and 330 km (the center of the plane lies at ~290-km depth). To compare with the observed signals, we applied the same 1,200-km scale wavelet filtering and the optimal angular analysis, averaging the modeled gravity gradient signals of amplitude above 0.010 mEötvös simultaneously found in the two ranges of azimuthal sensitivity Az_1 and Az_2. With a slip 1.3 times larger than in this previous paper, the modeled variations (Figure E1) show a good global agreement with the observed ones (Figure 4c).

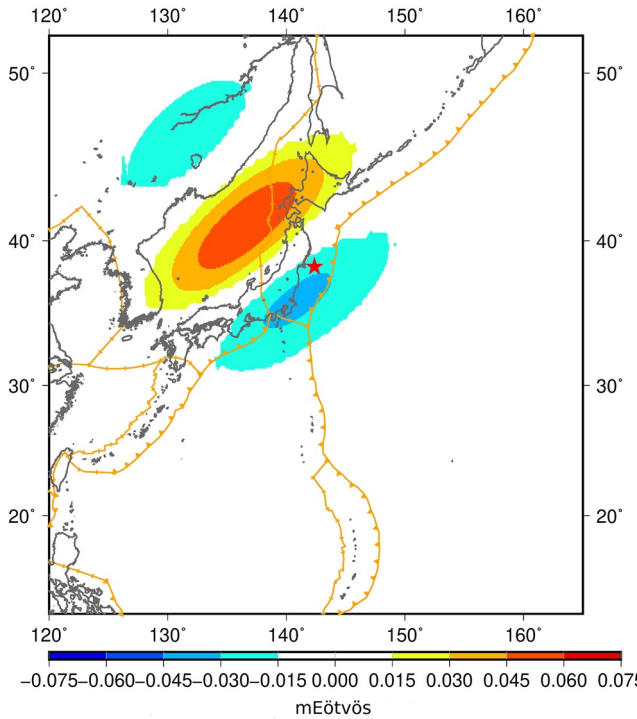

Figure E1. Modeled $\phi\phi$ gravity gradients (1,200-km scale, optimal analysis) from the preseismic normal faulting model of Panet et al. (2018). The amount of slip is increased to 52-cm to fit the GRACE signal shown in Main Figure 4c.

Data Availability Statement

The GRGS03 gravity field solutions and their dealiasing products are available at: https://grace.obs-mip.fr/variable-models-grace-lageos/grace-solutions-release-03/ and at: https://grace.obs-mip.fr/dealiasing_and_tides/dealiasing/. The CSR06 gravity field solutions and their dealiasing products are available at: http://icgem.gfz-potsdam.de/series and at: https://isdc.gfz-potsdam.de/grace-isdc/grace-gravity-data-and-documentation/. The softwares developed by the authors to perform the multiscale gravity gradient analysis and the clusters/overlap analysis are available at https://doi.org/10.6084/m9.figshare.20255679, https://doi.org/10.6084/m9.figshare.20255487, and https://doi.org/10.6084/m9.figshare.20267925.

Acknowledgments
This work was supported by CNES. It is based on observations from the GRACE satellites. We thank Stéphane Bourgogne for his kind support regarding the GRACE geoid models destriping and dealiasing products, including sharing the DDK filtering software. We thank Gilles Métris for providing us the numerical code of differentiation of the spherical harmonics in cartesian coordinates, based on Métris et al. (1998), and Georges Balmino for sharing numerical code to compute spherical harmonics. We thank two anonymous reviewers for their careful reviews, which contributed to improve this manuscript. The authors used the GMT software (Wessel & Smith, 1991) for plotting. This study contributes to the IdEx Université de Paris ANR-18-IDEX-0001.

References

Astiz, L., Lay, T., & Kanamori, H. (1988). Large intermediate-depth earthquakes and the subduction process. *Physics of the Earth and Planetary Interiors*, *53*(1–2), 80–166. https://doi.org/10.1016/0031-9201(88)90138-0

Bedford, J. R., Moreno, M., Deng, Z., Oncken, O., Schurr, B., John, T., et al. (2020). Months-long thousand-kilometre-scale wobbling before great subduction earthquakes. *Nature*, *580*(7805), 628–635.

Bettadpur, S. (2018a). Gravity recovery and climate experiment. Level-2 gravity field product user handbook (Tech. Rep. 327-734, pp. 1–21). GRACE.

Bettadpur, S. (2018b). *Gravity recovery and climate experiment. UTCSR level-2 processing standards document* (Tech. Rep. 327-742, pp. 1–16). GRACE.

Bird, P. (2003). An updated digital model of plate boundaries. *Geochemistry, Geophysics, Geosystems*, *4*(3), 1027. https://doi.org/10.1029/2001GC000252

Blöschl, G., & Sivapalan, M. (1995). Scale issues in hydrological modelling: A review. *Hydrological Processes*, *9*(3–4), 251–290.

Boening, C., Willis, J. K., Landerer, F. W., Nerem, R. S., & Fasullo, J. (2012). The 2011 la Niña: So strong, the oceans fell. *Geophysical Research Letters*, *39*, L19602. https://doi.org/10.1029/2012GL053055

Bouchon, M., Marsan, D., Durand, V., Campillo, M., Perfettini, H., Madariaga, R., & Gardonio, B. (2016). Potential slab deformation and plunge prior to the Tohoku, Iquique and Maule earthquakes. *Nature Geoscience*, *9*(5), 380–383. https://doi.org/10.1038/ngeo2701

Bouih, M., Panet, I., Remy, D., Longuevergne, L., & Bonvalot, S. (2022). Deep mass redistribution prior to the 2010 mw 8.8 maule (Chile) earthquake revealed by grace satellite gravity. *Earth and Planetary Science Letters*, *584*, 117465. https://doi.org/10.1016/j.epsl.2022.117465

Bruinsma, S., Lemoine, J.-M., Biancale, R., & Valès, N. (2010). CNES/GRGs 10-day gravity field models (release 2) and their evaluation. *Advances in Space Research*, *45*(4), 587–601. https://doi.org/10.1016/j.asr.2009.10.012

Carrère, L., & Lyard, F. (2003). Modeling the barotropic response of the global ocean to atmospheric wind and pressure forcing-comparisons with observations. *Geophysical Research Letters*, *30*(6), 1275. https://doi.org/10.1029/2002GL016473

Chao, B., & Liau, J. (2019). Gravity changes due to large earthquakes detected in grace satellite data via empirical orthogonal function analysis. *Journal of Geophysical Research: Solid Earth*, *124*, 3024–3035. https://doi.org/10.1029/2018JB016862

Chen, J., Pekker, T., Wilson, C. R., Tapley, B., Kostianoy, A., Cretaux, J.-F., & Safarov, E. (2017). Long-term Caspian Sea level change. *Geophysical Research Letters*, *44*, 6993–7001. https://doi.org/10.1002/2017GL073958

Chen, J., Wilson, C. R., & Tapley, B. D. (2010). The 2009 exceptional Amazon flood and interannual terrestrial water storage change observed by GRACE. *Water Resources Research*, *46*, W12526. https://doi.org/10.1029/2010WR009383

Dee, D. P., Uppala, S. M., Simmons, A. J., Berrisford, P., Poli, P., Kobayashi, S., et al. (2011). The era-interim reanalysis: Configuration and performance of the data assimilation system. *Quarterly Journal of the Royal Meteorological Society*, *137*(656), 553–597. https://doi.org/10.1002/qj.828

Dmowska, R., Rice, J. R., Lovison, L. C., & Josell, D. (1988). Stress transfer and seismic phenomena in coupled subduction zones during the earthquake cycle. *Journal of Geophysical Research*, *93*(B7), 7869–7884. https://doi.org/10.1029/JB093iB07p07869

Dobslaw, H., Bergmann-Wolf, I., Dill, R., Poropat, L., Thomas, M., Dahle, C., et al. (2017). A new high-resolution model of non-tidal atmosphere and ocean mass variability for de-aliasing of satellite gravity observations: AOD1B RL06. *Geophysical Journal International*, *211*(1), 263–269. https://doi.org/10.1093/gji/ggx302

Fasullo, J. T., Boening, C., Landerer, F. W., & Nerem, R. S. (2013). Australia's unique influence on global sea level in 2010–2011. *Geophysical Research Letters*, *40*, 4368–4373. https://doi.org/10.1002/grl.50834

Forootan, E., & Kusche, J. (2012). Separation of global time-variable gravity signals into maximally independent components. *Journal of Geodesy*, *86*, 477–497. https://doi.org/10.1007/s00190-011-0532-5

Gégout, P., Lyard, F., & Lemoine, J.-M. (2009). Background models used in geodetic data processing. In *IAG/GGOS workshop: Towards a roadmap for future satellite gravity missions*, September 30, 2009.

Gloor, M., Brienen, R. J., Galbraith, D., Feldpausch, T. R., Schöngart, J., Guyot, J.-L., et al. (2013). Intensification of the Amazon hydrological cycle over the last two decades. *Geophysical Research Letters*, *40*, 1729–1733. https://doi.org/10.1002/grl.50377

Haralick, R. M., & Shapiro, L. G. (1992). Computer and robot vision. In *Binary machine vision: Thresholding and segmentation* (Vol. 1, Chap. 2, pp. 28–48). Addison-Wesley.

Hasegawa, A., & Yoshida, K. (2015). Preceding seismic activity and slow slip events in the source area of the 2011 mw 9.0 Tohoku-oki earthquake: A review. *Geoscience Letters*, *2*(1), 1–13. https://doi.org/10.1186/s40562-015-0025-0

Ito, Y., Hino, R., Kido, M., Fujimoto, H., Osada, Y., Inazu, D., et al. (2013). Episodic slow slip events in the Japan subduction zone before the 2011 Tohoku-Oki earthquake. *Tectonophysics*, *600*, 14–26. https://doi.org/10.1016/j.tecto.2012.08.022

Jungclaus, J., Fischer, N., Haak, H., Lohmann, K., Marotzke, J., Matei, D., et al. (2013). Characteristics of the ocean simulations in the Max Planck institute ocean model (MPIOM) the ocean component of the MPI-Earth system model. *Journal of Advances in Modeling Earth Systems*, *5*, 422–446. https://doi.org/10.1002/jame.20023

Kaula, W. M. (1966). *Theory of satellite geodesy* (p. 345). Blaisdell Publ. Co.

Kusche, J., Schmidt, R., Petrovic, S., & Rietbroek, R. (2009). Decorrelated GRACE time-variable gravity solutions by GFZ, and their validation using a hydrological model. *Journal of Geodesy*, *83*(10), 903–913. https://doi.org/10.1007/s00190-009-0308-3

Lemoine, J.-M., Bourgogne, S., Biancale, R., Bruinsma, S., & Gégout, P. (2016). CNES/GRGS solutions: Focus on the inversion process. In *Grace science team meeting, a1-02*.

Lemoine, J.-M., Bruinsma, S., Loyer, S., Biancale, R., Marty, J.-C., Perosanz, F., & Balmino, G. (2007). Temporal gravity field models inferred from GRACE data. *Advances in Space Research*, *39*(10), 1620–1629. https://doi.org/10.1016/j.asr.2007.03.062

Mavrommatis, A. P., Segall, P., & Johnson, K. M. (2014). A decadal-scale deformation transient prior to the 2011 mw 9.0 Tohoku-oki earthquake. *Geophysical Research Letters*, *41*, 4486–4494. https://doi.org/10.1002/2014GL060139

Métris, G., Xu, J., & Wytrzyszczak, I. (1998). Derivatives of the gravity potential with respect to rectangular coordinates. *Celestial Mechanics and Dynamical Astronomy*, *71*, 137–151.

Mogi, K. (1973). Relationship between shallow and deep seismicity in the Western Pacific region. *Tectonophysics*, *17*(1–2), 1–22. https://doi.org/10.1016/0040-1951(73)90062-0

Mogi, K. (2004). Deep seismic activities preceding the three large 'shallow' earthquakes off South-East Hokkaido, Japan—The 2003 Tokachi-oki earthquake, the 1993 Kushiro-oki earthquake and the 1952 Tokachi-oki earthquake. *Earth Planets and Space*, *56*(3), 353–357. https://doi.org/10.1186/BF03353064

Nishikawa, T., & Ide, S. (2018). Recurring slow slip events and earthquake nucleation in the source region of the M 7 Ibaraki-Oki earthquakes revealed by earthquake swarm and foreshock activity. *Journal of Geophysical Research: Solid Earth*, *123*, 7950–7968. https://doi.org/10.1029/2018JB015642

Obara, K., & Kato, A. (2016). Connecting slow earthquakes to huge earthquakes. *Science*, *353*(6296), 253–257. https://doi.org/10.1126/science.aaf1512

Panet, I. (2018). An analysis of gravitational gradients in rotated frames and their relation to oriented mass sources. *Journal of Geophysical Research: Solid Earth*, *123*, 11062–11090. https://doi.org/10.1029/2018JB016717

Panet, I., Bonvalot, S., Narteau, C., Remy, D., & Lemoine, J.-M. (2018). Migrating pattern of deformation prior to the Tohoku-Oki earthquake revealed by GRACE data. *Nature Geoscience*, *11*(5), 367–373. https://doi.org/10.1038/s41561-018-0099-3

Ray, R., & Luthcke, S. (2006). Tide model errors and grace gravimetry: Towards a more realistic assessment. *Geophysical Journal International*, *167*(3), 1055–1059. https://doi.org/10.1111/j.1365-246x.2006.03229.x

Ruiz, S., Metois, M., Fuenzalida, A., Ruiz, J., Leyton, F., Grandin, R., et al. (2014). Intense foreshocks and a slow slip event preceded the 2014 Iquique Mw 8.1 earthquake. *Science*, *345*(6201), 1165–1169. https://doi.org/10.1126/science.1256074

Schwartz, S. Y., & Rokosky, J. M. (2007). Slow slip events and seismic tremor at circum-Pacific subduction zones. *Reviews of Geophysics*, *45*, RG3004. https://doi.org/10.1029/2006RG000208

Shahrisvand, M., Akhoondzadeh, M., & Sharifi, M. A. (2014). Detection of gravity changes before powerful earthquakes in grace satellite observations. *Annals of Geophysics*, *57*(5), A0543

Smith, S. (1998). The scientist & engineer's guide to digital signal processing (Chap. 15, Moving Average Filters). California Technical Publishing.

Socquet, A., Valdes, J. P., Jara, J., Cotton, F., Walpersdorf, A., Cotte, N., et al. (2017). An 8 month slow slip event triggers progressive nucleation of the 2014 Chile megathrust. *Geophysical Research Letters*, *44*, 4046–4053. https://doi.org/10.1002/2017GL073023

Tapley, B. D., Bettadpur, S., Ries, J. C., Thompson, P. F., & Watkins, M. M. (2004). GRACE measurements of mass variability in the Earth system. *Science*, *305*(5683), 503–505. https://doi.org/10.1126/science.1099192

Trenberth, K. E., & Fasullo, J. T. (2012). Climate extremes and climate change: The Russian heat wave and other climate extremes of 2010. *Journal of Geophysical Research*, *117*, D17103. https://doi.org/10.1029/2012JD018020

Ueda, H., Amagai, Y., & Hayasaki, M. (2017). South-coast cyclone in Japan during el niño-caused warm winters. *Asia-Pacific Journal of Atmospheric Sciences*, *53*(2), 287–293. https://doi.org/10.1007/s13143-017-0025-4

Ueda, H., Kibe, A., Saitoh, M., & Inoue, T. (2015). Snowfall variations in Japan and its linkage with tropical forcing. *International Journal of Climatology*, *35*(6), 991–998. https://doi.org/10.1002/joc.4032

van Dijk, A. I. J. M., Beck, H. E., Crosbie, R. S., de Jeu, R. A. M., Liu, Y. Y., Podger, G. M., et al. (2013). The millennium drought in southeast Australia (2001–2009): Natural and human causes and implications for water resources, ecosystems, economy, and society. *Water Resources Research*, *49*, 1040–1057. https://doi.org/10.1002/wrcr.20123

Waddell, P., Thomas, P., & Findlater, P. (2012). A report on the gascoyne river catchment following the 2010/11 flood events. *Resource Management Technical Report*, *382*, 1–91.

Wang, L., & Bürgmann, R. (2019). Statistical significance of precursory gravity changes before the 2011 Mw 9.0 Tohoku-Oki earthquake. *Geophysical Research Letters*, *46*, 7323–7332. https://doi.org/10.1029/2019GL082682

Wessel, P., & Smith, W. H. (1991). Free software helps map and display data. *Eos, Transactions American Geophysical Union*, *72*(41), 441–446. https://doi.org/10.1029/90EO00319

Yokota, Y., & Koketsu, K. (2015). A very long-term transient event preceding the 2011 Tohoku earthquake. *Nature Communications*, *6*(1), 1–5. https://doi.org/10.1038/ncomms6934